

1 **How much water is there within calcium silicate hydrates? Probing**
2 **water dynamics by Inelastic Neutron Scattering and Molecular**
3 **Dynamics Simulations**

4 Zhanar Zhakiyeva, Valérie Magnin, Agnieszka Poulain, Sylvain Campillo, María P. Asta, Rogier Besselink,
5 Stéphane Gaboreau, Francis Claret, Sylvain Grangeon, Svemir Rudic, Stéphane Rols, Mónica Jiménez-Ruiz,
6 Ian C. Bourg, Alexander E.S. Van Driessche, Gabriel J. Cuello, Alejandro Fernández-Martínez

7 **Corresponding Authors**

8 Zhanar Zhakiyeva - University of Grenoble Alpes, University of Savoie Mont Blanc, CNRS, IRD, IFSTTAR,
9 ISTERre, 38000 Grenoble; Institut Laue-Langevin, 38042 Grenoble, France; Department of Chemical and
10 Materials Engineering, School of Engineering and Digital Sciences, Nazarbayev University, Kabanbay Batyr
11 Ave. 53, Astana, 010000, Kazakhstan Phone: +77780665182; Email: zhanar.zhakiyeva@gmail.com

12 Alejandro Fernández-Martínez – University of Grenoble Alpes, University of Savoie Mont Blanc, CNRS, IRD,
13 IFSTTAR, ISTERre, 38000 Grenoble, France; Phone: +33(0)476635197; Email: alex.fernandez-
14 martinez@univ-grenoble-alpes.fr

15 Ian C. Bourg – Department of Civil and Environmental Engineering and High Meadows Environmental
16 Institute, Princeton University, Princeton, New Jersey 08544, United States; Email: bourg@princeton.edu

17 Alexander E. S. Van Driessche – University of Grenoble Alpes, University of Savoie Mont Blanc, CNRS, IRD,
18 IFSTTAR, ISTERre, 38000 Grenoble, France; Instituto Andaluz de Ciencias de la Tierra (IACT), CSIC –
19 University of Granada, Armilla, Granada E-18100, Spain; Email: alexander.vd@csic.es

20 **Authors**

21 Gabriel J. Cuello - Institut Laue-Langevin, 38042 Grenoble, France;

22 Valérie Magnin – University of Grenoble Alpes, University of Savoie Mont Blanc, CNRS, IRD, IFSTTAR,
23 ISTERre, 38000 Grenoble;

24 Sylvain Campillo – University of Grenoble Alpes, University of Savoie Mont Blanc, CNRS, IRD, IFSTTAR,
25 ISTERre, 38000 Grenoble;

26 Svemir Rudic - ISIS Neutron & Muon Source, STFC Rutherford Appleton Laboratory, Chilton, Didcot,
27 Oxfordshire OX11 0QX, U.K.;

28 Mónica Jiménez-Ruiz - Institut Laue-Langevin, 38042 Grenoble, France;

29 Stéphane Rols - Institut Laue-Langevin, 38042 Grenoble, France;

30 Agnieszka Poulain – University of Grenoble Alpes, University of Savoie Mont Blanc, CNRS, IRD, IFSTTAR,
31 ISTERre, 38000 Grenoble;

32 Rogier Besselink – University of Grenoble Alpes, University of Savoie Mont Blanc, CNRS, IRD, IFSTTAR,
33 ISTERre, 38000 Grenoble;

34 Stéphane Gaboreau – BRGM, Orléans Cedex 2 F-45060, France;

35 Sylvain Grangeon – BRGM, Orléans Cedex 2 F-45060, France;

36 Francis Claret – BRGM, Orléans Cedex 2 F-45060, France;

37 **KEYWORDS**

38 Interfacial water; C-(A)-S-H; inelastic neutron scattering; water dynamics; nanoporous vs bulk-
39 liquid-like water; molecular dynamics simulations; low CO₂ cements;

40 **1 ABSTRACT**

41 Calcium-silicate-hydrate (C-S-H) is a disordered, nanocrystalline material, acting as a primary
42 binding phase in Portland cement. C-S-H and C-A-S-H (an Al-bearing substitute present in low-
43 CO₂ cement) contain thin films of water on the interfaces and inside the nanopores. Water
44 controls chemical and mechanical properties of C-S-H, including drying shrinkage, ion transport,
45 creep, and thermal behavior. Therefore, obtaining a fundamental understanding of their
46 properties is essential. We applied a combination of inelastic incoherent neutron scattering and
47 molecular dynamics simulations to unravel the water dynamics in synthetic C-(A)-S-H
48 conditioned at five hydration states (from dry to fully hydrated) and with three Ca/Si ratios (0.9,
49 1, and 1.3). Our results converge towards a picture where the evolution from thin layers of
50 adsorbed water to bulk capillary water is dampened by the structure of C-(A)-S-H, in particular
51 by the availability of Ca²⁺ sites which keep the water in the form of structured surface layers.

52 **2 INTRODUCTION**

53 Cement paste is a multiphase material containing an extensive network of pores of different sizes.
54 Water, either in bulk form or adsorbed at the surfaces of the different cement phases, is
55 omnipresent [1]. The most important phase in cement is calcium-silicate-hydrate (C-S-H) and its
56 Al-bearing analog, present in low-CO₂ cement calcium-aluminum-silicate-hydrate (C-A-S-H). The
57 C-(A)-S-H phase itself is a nanocrystalline and disordered material with varying Ca/Si ratio and
58 water content and distribution. Not surprisingly, water plays a crucial role as it directly influences
59 the mechanical properties of cement, such as shrinkage, creep, and strength of concrete
60 structures [2], and fluid and solute transport processes that control cement geochemical
61 alteration and durability [3]. The detailed properties of cement pore water, however, remain
62 challenging to characterize because of the complex, heterogeneous, and nanoporous structure of
63 the material [4–6]. Hence, understanding water dynamics in cement systems remains a
64 fundamental topic of interest [7–11].

65 Previous experimental studies of the dynamics of water have mostly focused on the entire cement
66 paste, using different spectroscopic techniques that access different energy and spatial domains.
67 For example, Nuclear Magnetic Resonance provides information about the types of water, by
68 probing the local environment of the proton, and about its relaxation and exchange dynamics
69 [6,9,10,12–14]. Infra-red and Raman spectroscopies are sensitive to the stretching vibrational
70 modes of water, yielding information about the local environment of water [7,15]. Broadband
71 Dielectric Spectroscopy accesses water motion regimes in different sized pores by probing its
72 dielectric properties [1,16].

73 Inelastic neutron scattering (INS) [3,17–19] and Quasielastic Neutron Scattering (QENS) [3,19–
74 21] also have been widely applied to probe the dynamics of water in cementitious materials and
75 other confined water systems ranging from Vycor glass [22], to chalk [23], silica glass [24], and
76 clay minerals [25]. These methods probe time domains from nano- to picoseconds and spatial
77 domains from 0.1 to 10 nm, thus allowing the study of water rotational and translational
78 dynamics (diffusion, exchange between different environments at interfaces and in nanopores).
79 INS experiments performed on cement pastes under varying relative humidity (RH) conditions
80 have been found to distinguish interfacial/interlayer water [3,19], translations of water
81 molecules [26,27], translational dynamics of portlandite hydroxyl ions [17,18], and librational
82 modes of water (H-bond hindered rotations of water molecules).

83 Atomistic simulation methods, including notably molecular dynamics (MD) [28–30] simulations,
84 similarly can probe the dynamics of water in confined systems over time scales of nano to
85 femtoseconds and length scales of 0.1 to 10 nm, allowing direct comparisons with experimental
86 results from ^1H NMR, INS, QENS, and other experimental techniques. For example, a classical MD
87 study by Kalinichev et al. [31] revealed diffusion coefficients of $5.0 \times 10^{-11} \text{ m}^2/\text{s}$ for water in the
88 tobermorite (a natural crystalline analog of C-S-H [32]) and $6.0 \times 10^{-10} \text{ m}^2/\text{s}$ for water on the
89 external interfaces, in agreement with QENS experimental results [12,33].

90 Experimental and computational studies using the methods outlined above have converged
91 towards an identification of three water populations in cement paste with different dynamical
92 properties: (i) bulk-like water that is weakly bound and evaporates at around 100°C , which is
93 found in so-called gel pores larger than 3 nm in diameter; (ii) multilayer interfacial water found
94 within 1 nm (~ 3 water layers) from the C-(A)-S-H surfaces and; (iii) chemically bound water that
95 includes interlayer and strongly bound interfacial water and hydroxyls of Si-OH and Ca-OH
96 groups. A characteristic of these studies is that they have been performed on cement pastes
97 [34,35], and many date back 10 to 20 years when limited instrumental resolution obstructed a
98 detailed data interpretation [17,19,21,36]. These studies were instrumental in revealing the
99 complexity of C-(A)-S-H systems, including variability in the abundance of different phases and

100 different water populations. However, their use of comparatively ‘macroscopic’ approaches in
101 sample preparation has proved limiting in establishing a detailed molecular level understanding
102 of water in the pores or on the surfaces of the C-(A)-S-H phase of cement. In short, new
103 mechanistic understanding of the role that water plays in cement phase requires approaches that
104 can isolate water dynamics in the C-(A)-S-H phase.

105 In this work, we present an Inelastic Incoherent Neutron Scattering (IINS) investigation of water
106 in hydrated synthetic C-(A)-S-H complemented with MD simulations of water dynamics in the
107 same system using our recently developed C-S-H model [37]. IINS is a vibrational spectroscopic
108 method that is extremely sensitive to hydrogen atom vibrations due to the very large incoherent
109 scattering cross section of the H atom compared to other atoms. Consequently, it is ideal for
110 studying water dynamics, providing access to a wide range of water vibrational modes across the
111 spectroscopic range, even the librational modes that cannot be measured with other techniques
112 (for instance IR spectroscopy) because the signal is masked. The IINS method offers several
113 advantages compared to traditional spectroscopic techniques like Raman and IR spectroscopy: i)
114 Due to the interaction of neutrons with the nuclei, no selection rules apply, enabling access to *all*
115 vibrational modes; ii) Neutron scattering methods are non-destructive, preserving the integrity
116 of the sample for further analysis; and iii) Experimental neutron spectroscopy data can be readily
117 complemented and interpreted by atomistic level simulations, including MD simulations.

118 We carried out IINS experiment, for C-(A)-S-H at three Ca/Si ratios (0.9, 1, and 1.3) and five
119 hydration states (fully hydrated, oven-dried, conditioned at 55% and 98% RH levels, and
120 desorbed/dried at 11% RH). First, we examine the impact of varying Ca/Si ratios and RH levels
121 on our experimental IINS data. This analysis sheds light on how these factors influence the water
122 dynamics within the C-(A)-S-H structure. Next, we utilize the generalized density of states (GDOS)
123 predicted by MD simulations to deepen our interpretation of our experimental data and reveal
124 the complex interplay between structural parameters and observed spectral features. Finally, we
125 evaluate the diffusion coefficients of interfacial and interlayer water and subsequently compare
126 them to the diffusion constant of bulk water. This comparison provides insights into the differing
127 mobility behaviors of water in distinct compartments within the C-(A)-S-H system.

128 **3 MATERIALS AND METHODS**

129 **3.1 Sample preparation**

130 C-S-H samples of Ca/Si = 1, 1.2, and 1.3 were synthesized by reacting calcium oxide and fumed
131 silica in water inside an N₂ wet glove box. Calcium oxide was obtained by calcination of CaCO₃
132 (Sigma-Aldrich, Fluka, Bioultra) at 1000 °C for 18 h and stored in a vacuum desiccator until usage.
133 Fumed silica SiO₂ (Sigma-Aldrich, Aerosil 200) was placed in an oven at 40 °C for ~24 h to remove
134 physisorbed water prior to each experiment. Deionized water was boiled and degassed with N₂

135 gas to remove all dissolved CO₂. The quantities of calcium oxide and fumed silica required to
136 prepare C-S-H of predetermined stoichiometry were calculated using the method reported by
137 Haas and Nonat [38] (Table S1 in the Supporting Information). Samples were left reacting under
138 stirring conditions for ~1 month in High Density Polyethylene (HDPE) bottles inside a wet N₂
139 glove box, then filtered using Millipore® filter paper (0.22 μm, GSW1 UM), and the wet C-S-H
140 residue was left to dry inside a glove-box for ~12 h. The C-A-S-H samples with Ca/Si = 0.9, and
141 Al/Si = 0.1, were synthesized following the protocol that can be found elsewhere [39]. We use C-
142 (A)-S-H when we refer both to C-S-H and C-A-S-H samples. Aliquots of these C-(A)-S-H samples
143 were preserved and will be referred to as fully-hydrated or 'FH' C-(A)-S-H.

144 The remaining portion of each FH C-(A)-S-H sample was oven-dried at 40 °C in a vacuum oven for
145 ~24 h. Based on previous studies [7] and our own experience, this temperature is not sufficient
146 to remove highly-bound water even under conditions of dynamic vacuum, but it is enough to
147 evaporate the majority of bulk capillary-pore and adsorbed gel-pore water. A part of these
148 samples was stored separately and is referred to as oven-dried or 'OD' C-(A)-S-H.

149 The remainder of each sample was exposed to a controlled RH of 55% or 98% using saturated
150 salt solutions of Mg(NO₃)₂·6H₂O and K₂SO₄, respectively (Fig. S.1 in the Supporting Information).
151 The equilibration times for C-S-H samples lasted 1 week, and for C-A-S-H samples 1 month. The
152 different equilibration times were due to the availability of the neutron beamtime. We note that,
153 ideally experiments involving water adsorption in C-(A)-S-H should be done in the same
154 timeframe to eliminate the equilibration time effect. We refer to these C-(A)-S-H as '55RH' and
155 '98RH' samples. Finally, a portion of each 98RH C-(A)-S-H sample was stored inside a vacuum
156 desiccator containing silica beads to remove any adsorbed or bulk water [40]. We named these
157 samples desiccator-dried or 'DD' samples.

158 Following these conditioning protocols, we obtained C-S-H samples labeled CSH_Ca/Si_%RH,
159 where %RH is the relative humidity value at which they were conditioned. The C-A-S-H samples
160 were labeled CASH_Ca/Si_%RH. In the text, we refer to 'wet' (FH, 98RH) and 'dry' (55RH, OD, DD)
161 C-(A)-S-H samples. As C-(A)-S-H is sensitive to atmospheric CO₂, all synthesis and conditioning
162 processes were performed under an inert gas atmosphere of N₂.

163 **3.2 Sample characterization**

164 **3.2.1 Inductively coupled plasma - atomic emission spectrometry (ICP-AES).**

165 Ca/Si ratios were determined using ICP-AES (Varian 720ES Agilent). The C-(A)-S-H particles (5-
166 10 mg) were dissolved by adding of concentrated 14 M HNO₃ (distilled) and 28 M HF (47-51%,
167 Trace Metal™, for Trace Metal Analysis, Fisher Chemical) acids, followed by heating the solution
168 for ~24h at ~80°C. The final step involved diluting with boric acid and ultrapure water up to 150
169 mL prior to the measurement.

170 **3.2.2 Water adsorption volumetry**

171 Water adsorption isotherms were obtained at 25 °C using a Belsorp-Max instrument by BEL
172 JAPAN Inc. A long acquisition time of at least 2 weeks was required due to the slow equilibrium
173 kinetics. Prior to the measurements, all samples were outgassed at 50 °C for 24 h under a residual
174 pressure of 4.652×10^{-5} Pa. The classical Brunauer–Emmett–Teller (BET) theory was used to
175 analyze the isotherms and derive the specific surface area (SSA) [41] (Table 1).

176 **3.2.3 Thermogravimetric analysis**

177 Thermogravimetric analysis (TGA, Mettler-Toledo TGA-DSC3+) was used to examine the thermal
178 decomposition and determine the water content of the C-(A)-S-H samples. The samples were
179 analyzed at a heating rate of 10°C/min up to 600°C in an N₂ environment with a flow rate of 20
180 mL/min. The samples were loaded in aluminum crucibles and were hermetically sealed with
181 aluminum caps inside a glove box or a glove bag filled with N₂ equilibrated at the same RH used
182 to condition the sample. The sample mass used for TGA analyses varied between 8 and 30 mg.
183 The amounts of water deduced from the TGA have been normalized per mass of C-S-H measured
184 at the end of the heating, at 600°C.

185 **3.2.4 Synchrotron X-Ray diffraction**

186 Synchrotron XRD measurements for the C-S-H samples were performed at the ID31 beamline of
187 the European Synchrotron Radiation Facility (ESRF) in Grenoble, France. Prior to analysis, C-(A)-
188 S-H samples were loaded into 1.5 mm (ID31) polyimide capillaries inside the glove bags, or wet
189 glove-box, at the same RH values. The capillaries were sealed airtight on both ends using a two-
190 part epoxy adhesive.

191 At the ID31 beamline, a monochromatic X-ray beam of 78 keV ($\lambda = 0.159 \text{ \AA}$) was used to obtain
192 scattering patterns of C-S-H samples. The data sets were collected using a PilatusX 2M CdTe
193 detector placed at a sample-to-detector distance of $d_1 = 1.226$ m to obtain scattering patterns with
194 a Q range of 0.1-6.2 \AA^{-1} . This allowed the measurement of the Bragg peak corresponding to the
195 interlayer distance of C-S-H. Data were automatically corrected for internal dark current. Two-
196 dimensional images of the scattered intensity were azimuthally integrated using the pyFAI
197 software package [42]. The pattern from the empty capillary was subtracted as a background.

198 The C-A-S-H samples were measured at the 11-ID-B beamline at the Advanced Photon Source,
199 Argonne National Laboratory. Samples were analyzed with a monochromatic X-ray beam of 58.6
200 keV ($\lambda = 0.2115 \text{ \AA}$). Data were collected with a Perkin Elmer XRD 1621 N ES detector and sample-
201 to-detector distance of $d = 0.799$ m to access a Q range of 0.2-10.4 \AA^{-1} . Data were automatically
202 corrected for internal dark current. Two-dimensional images of the scattered intensity were
203 azimuthally integrated using the GSAS II software package [43].

204 3.3 Inelastic Incoherent Neutron Scattering

205 The inelastic neutron scattering event involves both energy (E , cm^{-1}) and momentum ($|\mathbf{Q}|$, \AA^{-1})
206 transfer. The energy transfer (E_T) is defined as $E_T = E_i - E_f$ where i and f refer to the incident and
207 final neutron energy values, respectively. The momentum transfer is given by $\mathbf{Q} = \mathbf{k}_i - \mathbf{k}_f$, where
208 the absolute value of the wavevector \mathbf{k} is defined as $|\mathbf{k}| = \frac{2\pi}{\lambda}$, and λ is the wavelength of the
209 neutron. IINS captures vibrational modes across a wide energy range, from the microwave to the
210 ultraviolet regions. In this paper, we are mostly interested in the region spanning from
211 microwave to mid-infrared, i.e., from 20 to 2000 cm^{-1} . Providing that the final wavevector, k_f , is
212 much smaller than the incident wavevector k_i , the observed intensity is directly proportional to
213 the generalized density of states (GDOS), which in the case of hydrogenated samples is the
214 hydrogen partial density of states.

215 INS spectra of C-S-H samples with Ca/Si=1.2 and 1.3 were collected in the energy range from
216 133.3 to 1940 cm^{-1} (16.5 to 240 meV) with an energy resolution of $\Delta E/E \sim 2\text{-}3\%$ using the
217 indirect geometry spectrometer Lagrange (LARGE GRAPHITE ANALYSER FOR GENUINE EXCITATIONS)
218 secondary spectrometer at the hot source of high-flux reactor of the Institut Laue-Langevin (ILL),
219 France (doi:10.5291/ILL-DATA.7-04-167) [44,45]. A combination of two double focusing
220 monochromators was used to access the energy range: Cu(220) to access the intermediate
221 energies, and Si(311) for lower energies.

222 The energy transfer range was obtained by subtracting the final energy of 4.5 meV of
223 PolyGraphite (PG) analyzers from the experimentally obtained one. The samples were loaded into
224 hollow aluminum cells, which were sealed under RH conditions matching the preparation of each
225 of C-S-H samples. The INS spectra were collected at 10 K (to lower the Debye-Waller origin of the
226 damping of the high energy bands) for the samples, the empty holders, and the cryostat. The
227 background spectrum from the latter was subtracted from the raw INS spectra of the C-S-H
228 samples. The $S(Q, E)$ from Cu(220) and Si(311) reflecting planes were manually merged to obtain
229 the final $S(Q, \omega)$ in the range 133.3 to 1940 cm^{-1} . Data reduction was performed using LAMP
230 (Large Array Manipulation Program) software [46].

231 The INS spectra of C-S-H samples with Ca/Si = 1, and C-A-S-H samples with Ca/Si = 0.9 were
232 measured at 10 K using TOSCA spectrometer at the ISIS spallation Neutron and Muon Source
233 (Rutherford Appleton Laboratory, UK) [47,48]. TOSCA is an indirect geometry time-of-flight
234 spectrometer operating in the energy transfer ranges up to 8000 cm^{-1} with an $\Delta E/E$ resolution of
235 $\sim 1.25\%$. The samples were loaded in Al cells and sealed with In-wire under RH conditions
236 matching the preparation of the C-S-H samples. All manipulations were performed inside a wet
237 glove box or glove bags to prevent contamination by carbon dioxide. The Al cells were then

238 mounted on a center stick connected to a gas handling system. The INS signals from sample
239 scattered neutrons and empty Al cells were recorded by detectors both in forward and in
240 backward directions for about 4 hours per sample. The neutron beam size was approximately 40
241 mm x 40 mm. The resulting data were combined using Mantid software [49]. Inelastic signals
242 coming from the empty Al cells were subtracted for each sample, and the spectra were scaled by
243 sample mass. More precisely, spectra were normalized by initial sample mass, i.e., the mass of the
244 oven-dried C-S-H samples before conditioning at varying RH levels.

245 **3.4 Molecular Dynamics Simulations**

246 Atomistic simulations were performed at the Cori supercomputer at the National Energy
247 Research Scientific Computing Center (NERSC, USA) using the MD simulation code LAMMPS [50],
248 which solves Newton's equations of motion for many-particle systems interacting through
249 pairwise potentials. Interatomic interactions were described using the SPC water model [51], and
250 the CLAYFF model of mineral-water interactions [52,53]. The CLAYFF force field was chosen
251 because of its versatility and successful descriptions of various systems including clay minerals
252 [31,54–57], zeolites [58], and other phases [59–61], validated against the results of X-ray and
253 neutron scattering experiments [31,62], and a variety of other experimental techniques [63,64].

254 The structure of the C-S-H nanoparticle model is described in detail elsewhere [37] and is briefly
255 presented in Fig. S.2 in the Supporting Information. While we acknowledge the existence of the
256 C-S-H sheet model [65], for the purposes of this discussion whether the edges of the C-S-H particle
257 are chemically connected or not should have little or no impact on our results. The C-S-H model
258 used in our MD simulations is based on the colloidal model by Jennings [66], and it describes well
259 the structural characteristics of interfacial water [37].

260 We have used our C-S-H nanoparticle model at two hydration states: the 'dry' atomic model
261 named 'CSH-dry-NP' with $H_2O/Si = 1.35$ (molecules/molecules) and interlayer spacing $d_{001-MD} =$
262 $11.0(2)$ Å; and a fully hydrated state 'CSH-wet-NP' with $H_2O/Si = 38.5$ and interlayer spacing d_{001-}
263 $_{MD} = 13.0(2)$ Å [37]. Analyses of the MD simulation trajectories were performed using custom-
264 made Python codes over the frames from the production runs as input. The GDOS of the two
265 simulated systems were calculated using the Molecular Dynamics Analysis for Neutron Scattering
266 Experiments (MDANSE) python-based application [67].

267 **4 RESULTS AND DISCUSSION**

268 **4.1 Water content in C-(A)-S-H samples as a function of Ca/Si**

269 Calcium-(aluminium)-silicate-hydrates are well known to have varying stoichiometry depending
270 on the Ca/Si ratio, the hydration state of the sample, and the abundance of defects in the C-(A)-S-
271 H structure [68–70]. To discern these variations, we determined the water content and

272 distribution in our C-(A)-S-H samples at three Ca/Si ratios (0.9, 1, and 1.3), encompassing five
273 different hydration states and an additional sample of CSH_1.2_DD.

274 The total weight loss (from 25 to 600°C) qualified by TGA, which includes all water and hydroxyls
275 in the samples, is referred to here as ‘total water’ amount. The amount of bulk-like water is
276 quantified based on the first minimum of each dTG curve around 100°C (Fig. S.3 in the Supporting
277 Information). We note that this water classification is based on the energetics of water release
278 from C-(A)-S-H. Thus, bulk-like water is water that evaporates at around 100°C and is found
279 predominantly in large gel pores (>3 nm), but small amounts of bulk-like water are also found in
280 the ‘dry’ samples as remnant water inside the large pores.

281 **4.1.1 ‘Dry’ C-(A)-S-H samples (55RH, OD and DD)**

282 Results from the TGA experiments indicate similar amounts of water for all ‘dry’ C-(A)-S-H
283 samples (Fig. S.4 in the Supporting Information). The total amount of water in ‘dry’ C-(A)-S-H
284 were constant regardless of Ca/Si value and in accordance with the literature [71]. The average
285 quantity of total water for OD samples was about 18±2 wt.%. The d_{001} spacing values for OD
286 samples were about 0.6 Å lower than for DD samples, which can be explained by the more efficient
287 removal of interlayer water under vacuum.

288 The 55RH C-(A)-S-H samples contained about 20±2 wt.% of total water irrespective of Ca/Si
289 ratios. The results of WSI point to decreased amounts of adsorbed water with increasing Ca/Si
290 ratios (Fig. S.5 and S.6 in the Supporting Information). The WSI results show that the amount of
291 adsorbed water for CASH_0.9 was roughly 1.9 times larger than for CSH_1.3 and CSH_1 (Table 1).

292 Exposure of the 98RH samples to a desiccator environment (<11% RH) containing silica gel lead
293 to a reduction in total water content by 10-20 wt.% and to the transformation of these samples
294 into DD samples. At RH levels <11%, ‘drying’ of the interlayer also takes place [4,40,72], leading
295 to a contraction of the d_{001} values, observed through XRD (Fig. 1). The extent of C-(A)-S-H
296 interlayer space contraction is about 2.5 Å (Fig. S.7 in the Supporting Information), on average,
297 from ‘wet’ to ‘dry’ samples, consistent with the work of other researchers (who reported ~3 Å)
298 [7]. This value is roughly the size of a water molecule, which is complementary to the TGA data
299 showing a difference of about 1 H₂O/Si between the ‘dry’ and ‘wet’ C-(A)-S-H samples also
300 reported in the literature [7,70,71].

301 *Table 1. Summary of TGA, WSI, and XRD results for ‘wet’ and ‘dry’ C-(A)-S-H samples.*

Sample name	Total water (TGA / wt.%) (25-600°C)	Bulk-like water (dTG / wt.%) (~100°C)	Adsorbed water (WSI /mmol g ⁻¹ C-A-S-H)	SSA (m ² /g)	d_{001} -XRD (Å)
C-A-S-H. Ca/Si=0.9					
DD	16±2	1.8±2		353	12(2)

OD	19±2	3.4±2		11.9(2)
55RH	22±2	4.4±2	8.4	12.4(2)
98RH	36±2	13±2	22.3	13.7(2)
C-S-H. Ca/Si=1				
DD	15±2	1.4±2		180 11.6(2)
OD	17±2	1.3±2		10.6(2)
55RH	23±2	3.4±2	4.4	12(2)
98RH	27±2	7.1±2	20.3	12.3(2)
FH	28±2	10.5±2		13.1(2)
C-S-H. Ca/Si=1.2				
DD	16±2	1.5±2		177 10.6(2)
C-S-H. Ca/Si=1.3				
DD	16±2	0.7±2		135 10.4(2)
OD	17±2	1.1±2		9.8(2)
55RH	20±2	3.1±2	4.4	
98RH	24±2	6±2	14.1	11.9(2)
FH	26±2	6.9±2		11.5(2)

302

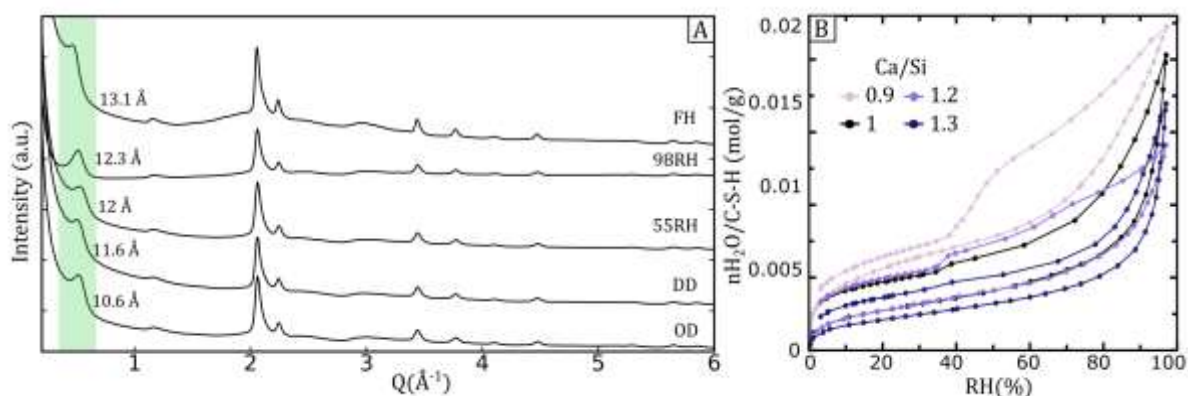
303 **4.1.2 'Wet' C-(A)-S-H samples (FH and 98RH)**

304 The TGA results revealed that fully-hydrated samples CSH_1_FH and CSH_1.3_FH contain 28±2,
 305 and 27±2 wt.% of total water, respectively. This total water consists primarily (mol/g_{dry-CSH}) of
 306 less strongly bound bulk-like capillary water, as indicated by intense dTG minima centered at
 307 100°C (Fig. S.3 in the Supporting Information). The FH samples have interlayers filled with water
 308 molecules, reflected in d_{001} values of 11.5 Å for CSH_1.3 and 13.1 Å for CSH_1 sample. These values
 309 are about 2 to 2.5 Å larger than for 'dry' C-(A)-S-H samples (Table 1).

310 WSI was used to calculate the specific surface areas of C-(A)-S-H accessible to water. According
 311 to the IUPAC classification [73], the water sorption isotherms belong to type II with an H3
 312 hysteresis type formed throughout the whole RH range (Fig. 1). A characteristic hysteresis
 313 between adsorption and desorption branches, and a sudden drop in the adsorbed amount at RH
 314 ~35% were observed for nearly all samples. The origin of the hysteresis is generally explained
 315 by the presence of 'ink bottle pores' that have narrow entrances to the pore, which are
 316 considerably smaller than the actual pore diameter [74]. The BET method [41] allows the
 317 calculation of the SSA from the adsorption branch at relative pressure levels from 0.05 to 0.3. The
 318 results show a clear decrease in SSA of C-(A)-S-H at increasing Ca/Si ratios (Table 1). For Ca/Si
 319 ratios from 0.9 to 1.3, the SSA decreases from 353 m²/g for CASH_0.9 to 135 m²/g for CSH_1.3.
 320 We note that the absolute values for surface areas of cement pastes and pure C-S-H vary widely
 321 depending on the adsorbate used, the drying technique, and the temperature of the sample
 322 [74,75].

323 The rewetting at 98% RH of the OD (oven-dried) samples proceeds through water populating the
324 interfaces and the interlayer [40], with the amount of adsorbed water depending on the
325 equilibration time [76]. The comparison of our WSI data with the data from Roosz et al. [8] show
326 that long exposure to RH > 95% leads to higher amounts of water being adsorbed on the C-(A)-S-
327 H surfaces, followed by capillary condensation in pores. This phenomenon results in varying
328 amounts of total water for 98RH C-(A)-S-H samples at varying Ca/Si ratios.

329 The TGA/dTG curves show that the proportions of bulk-like water to total water decrease from
330 CASH_0.9 to CSH_1 to CSH_1.3. Some part of the adsorbed water stays as multilayer interfacial
331 water, and some water enters the interlayers thus increasing d_{001} reflection values by 1.8 to 2 Å
332 (Table 1).



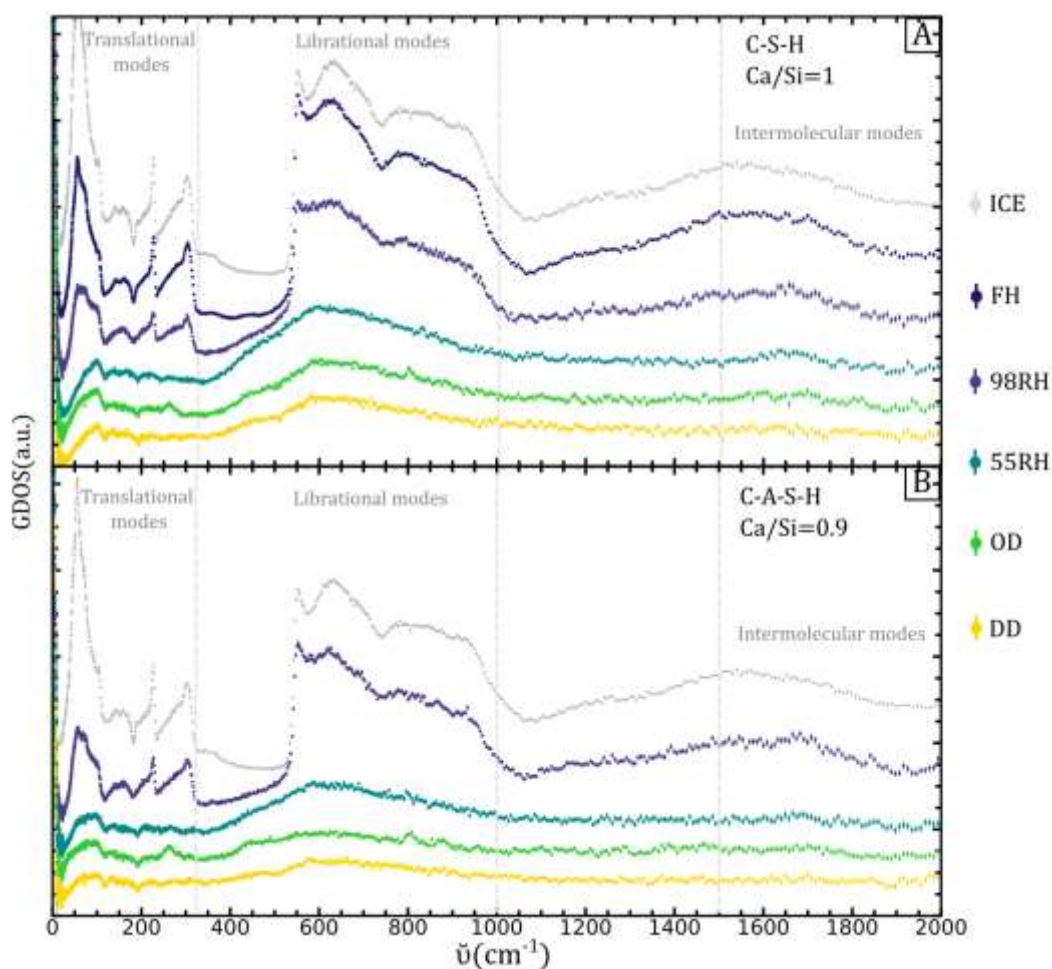
333
334 *Fig. 1. (A) X-ray diffraction patterns of CSH_1 sample showing changes in the d_{001} values with changing RH*
335 *levels: FH (fully hydrated), 98RH (conditioned under 98% RH), 55RH (conditioned under 55% RH), DD*
336 *(desiccator dried), OD (oven dried); (B) Water sorption isotherms of C-(A)-S-H samples showing the amounts*
337 *of adsorbed water at increasing RH values.*

338 4.2 Experimental IINS data

339 In this section 4.2 we detail the results of the IINS experiments that were used to probe the
340 dynamics of water in C-(A)-S-H samples with three Ca/Si ratios (0.9, 1, 1.3) at five hydration
341 levels. The integrated intensity of the IINS spectra (GDOS) is proportional to the total amount of
342 water and hydroxyls in the C-(A)-S-H samples.

343 4.2.1 Impact of RH level in CSH_1

344 A first comparison between the C-S-H and ice I_h spectra allow distinguishing the 'dry' C-S-H
345 samples (green-yellow curves) from the 'wet' C-S-H samples (blue curves) (Fig. 2). The former
346 contains only interlayer and interfacial water and have lower water content than the 'wet'
347 samples (as deduced from WSI, TGA and XRD data). The spectra resulting from the 'wet' C-S-H
348 samples contain bulk capillary pore water in addition to the interlayer and interfacial water.



349

350 *Fig. 2. Evolution of the generalized density of states (GDOS) of (A) CSH₁ samples; (B) and CASH_{0.9} samples*
 351 *with increasing hydration states. For the sake of clarity, all the spectra have been arbitrarily shifted along the*
 352 *GDOS axis. The spectra have been normalized to the water content of the sample in the beam. The translations*
 353 *of water molecules at 80, 226, and 305 cm⁻¹ (10, 28, and 38 meV) evident in samples containing bulk-like water*
 354 *(FH and 98RH) evolve into the dampened signal at 96 cm⁻¹ (12 meV) upon loss of water. Accordingly,*
 355 *librational edges evolve from the sharp vertical onset in FH samples into a rising slope in dry samples (55RH,*
 356 *OD, DD). The librational edges of 98RH samples contain features of bulk-like water and multilayer adsorbed*
 357 *water. Librational modes, which reflect the hydrogen bonding network, undergo changes in shape and*
 358 *intensity as they transition from an ice-like distribution to a broader triangular shaped distribution spanning*
 359 *a range of frequencies from 400 to 1000 cm⁻¹ (equivalent to 50 to 125 meV). The librational modes of drier*
 360 *samples (OD, DD) have lower intensities and librational edges shifted to lower energies than in the 55RH*
 361 *samples, reflecting their smaller water content and less extensive H-bonding network.*

362 The power spectra of ice Ih (grey curve in Fig. 2) can be broken down into three different regions:
 363 a low energy part representing the translational modes at 0-323 cm⁻¹ (0-40 meV); a librational
 364 region, which represents hindered rotations of H-bonded water molecules, is found between 444-
 365 968 cm⁻¹ (55-120 meV); the high frequency intramolecular vibrations, such as bending modes are
 366 observed at 1613 cm⁻¹ (200 meV) and O-H stretching modes at 3307 cm⁻¹ (410 meV) [77].

367 4.2.1.1 Lower energy modes (0-320 cm⁻¹)

368 The lower energy translational modes in ice Ih are characterized by the triangular features at 57
 369 cm⁻¹ (~7 meV) known as acoustic modes, and at 226 and 298 cm⁻¹ (28 and 37 meV) known as

370 optic modes. These modes involve the O-H stretch for a tetrahedral bonding motif in the ice lattice
371 [78]. The same translational modes are evident in the 'wet' C-S-H samples, with slightly lower
372 relative intensities than in ice Ih. On the other hand, the 'dry' C-S-H samples show a dramatic
373 change in the region of lower energies, with translational and acoustic modes attenuated and
374 shifted to higher frequencies. This signifies that the tetrahedrally ordered structure of the H-
375 bonding network is not present, meaning that the water molecules on the C-S-H surfaces have a
376 different local order than in ice Ih [79].

377 The behavior described above has been previously observed for water adsorbed at the solid-
378 water interfaces of other nanosystems [3,23,77,80–83]. In the case of cementitious materials,
379 previous INS studies have identified the peaks at around 80 and 242 cm^{-1} (10 and 30 meV) as
380 'fingerprints' of confined water. In computer simulations on supercooled water [84] and
381 experimental studies (at room temperature) on Vycor glasses [22,26], these peaks have been
382 attributed to the translational motions of water molecules inside the confining cage. Analogous
383 peaks are observed are at about 97 and 249 cm^{-1} (12 meV and 30.9 meV). The difference in peak
384 position relative to previous studies of cementitious materials could be due to the improved
385 resolution of the instruments or to the tendency of these peaks to shift and vary in spectral
386 intensity depending on the ions present in the system and the hydration state [83,85]. In our case,
387 we have assigned these peaks to the dangling hydrogens of strongly bound interfacial water
388 molecules, based on the calculated partial GDOS as will be explained later.

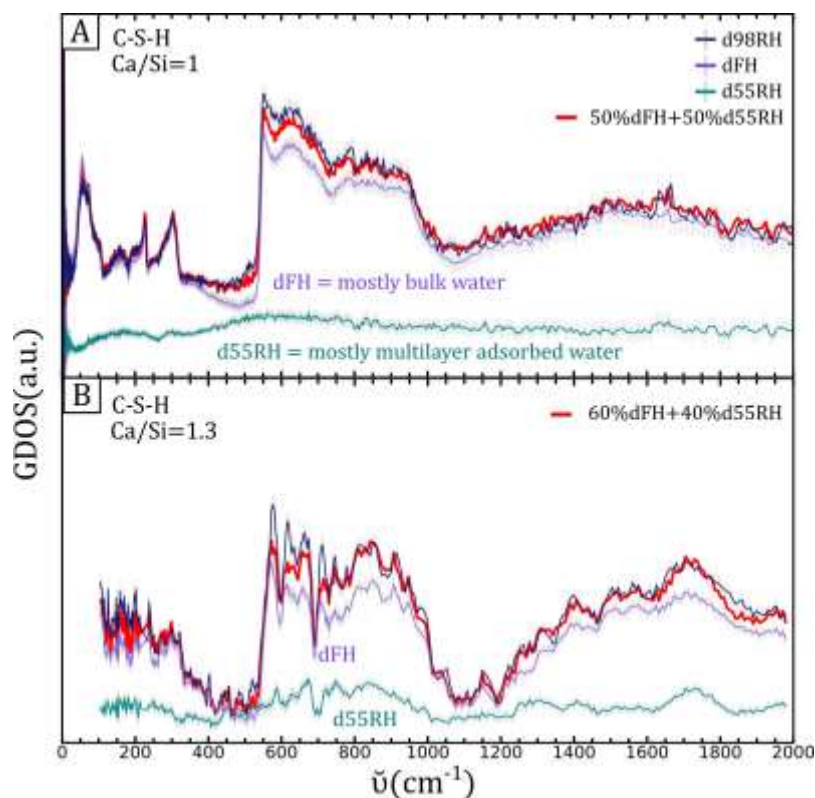
389 *4.2.1.2 Librational modes (300-1000 cm^{-1})*

390 The librational modes found between $\sim 300\text{-}1000 \text{ cm}^{-1}$ (37-124 meV) are very sensitive to the
391 strength of the hydrogen bonds. The librational modes include the rocking, twisting, and wagging
392 modes with their corresponding energies increasing accordingly (shown schematically in Fig. S.8
393 in the Supporting Information). However, the modes associated with different motions are
394 strongly coupled and cannot be readily deconvolved [85,86]. The librational edge represents the
395 start of the librational modes energies, with a sharper edge at the low frequency side signaling
396 the presence of a highly ordered structure with degeneration of some of these modes into a sharp
397 peak indicative of water forming an extensive H-bonding network.

398 The evolution of the shift of the librational edge as a function of the water content can be followed
399 by the changes observed from about 350 cm^{-1} (~ 43.3 meV) for 'dry' to nearly 520 cm^{-1} (~ 204
400 meV) for 'wet' C-S-H samples. The absence of a clear librational edge (a broken degeneracy of the
401 librational modes) similar to ice confirms the absence of bulk-like water in the 'dry' C-S-H
402 samples. Among the 'dry' C-S-H samples, the librational modes of the OD and DD samples show
403 shoulders at about 500 cm^{-1} (a convolution of the rocking, twisting, and wagging modes), while
404 the 55RH C-S-H sample shows a smoother and sharper edge, indicating the presence of more

405 water. This is in good agreement with the results of TGA, which show that CSH_1_55RH contains
406 35% and 40% more of total water than the OD and DD samples, respectively (Table 1).
407 Experimental [8] and computational [87] work has shown that at ~55% RH, C-S-H contains both
408 interlayer and multilayer adsorbed water.

409 The 'wet' C-S-H samples reveal a close resemblance to ice, showing that they contain bulk liquid-
410 like capillary pore water in addition to the interlayer and interfacial water. The CSH_1_98RH
411 incorporates less bulk water than the fully hydrated C-S-H sample as shown by the results of the
412 TGA and XRD experiments. Indeed, the start of the librational edge of CSH_1_98RH coincides with
413 that of CSH_1_55RH, followed by a sharp vertical rise coinciding with the librational edge of ice Ih
414 at around 500 cm⁻¹ (62 meV) shown in Fig. 2.A. The 'combined' edge of CSH_1_98RH shows that
415 the sample contains multilayer water, together with bulk capillary pore water. We performed the
416 linear combination fitting by taking two end members (dFH and d55RH) to fit C-S-H_98RH
417 samples. Both dFH and d55RH spectra are the results of the subtraction of OD from FH and 55RH
418 spectra, respectively. The subtraction of the OD spectrum aimed to remove most of the
419 contributions from interlayer and monolayer water, thus leaving predominantly bulk-liquid-like
420 water in dFH and multilayer adsorbed water in d55RH spectra (Table 1). The CSH_1_98RH
421 spectrum showed a good match to an evenly-weighted-sum of the dFH and d55RH spectra (Fig.
422 3.A). The fit results are in good accordance with the TGA data, showing that upon rewetting of the
423 CSH_1 sample at 98% RH, the water distributed as 52% of bulk-liquid-like water and 48%
424 multilayer adsorbed water.



425

426 *Fig. 3. Linear combination fittings of C-S-H_{98RH} samples: (A) Ca/Si = 1 best fit with 50% of dFH and 50% of*
 427 *d55RH samples; (B) Ca/Si=1.3 best fit with 60% of dFH and 40% of d55RH samples.*

428 4.2.1.3 Intramolecular modes (1500-4000 cm⁻¹)

429 At higher energies, we observe intramolecular modes including H-O-H bending modes at around
 430 1650 cm⁻¹ (205 meV) and O-H stretching modes at around 3600 cm⁻¹ (446 meV). The values of
 431 the former and the latter modes tend to shift to higher frequencies with increasing water content.
 432 In our case, this is not observed because both bending and stretching modes are difficult to
 433 distinguish from the background signals. There are several plausible explanations: first, at high
 434 energy transfers of IN1-Lagrange and TOSCA instruments (inverse geometry) the signal is
 435 dampened significantly. Secondly, the Debye-Waller effect i.e., the thermal fluctuations, at higher
 436 Q values substantially attenuate the intensity in the spectra. Experiments were performed at 10
 437 K to avoid most of thermal fluctuations. Finally, at higher Q ranges there is an increase in
 438 multiphonon intensity, which gives a rising background with increasing Q values.

439 4.2.2 Impact of RH levels in CASH_{0.9}

440 IINS spectra of CASH_{0.9} with different water contents are shown in Fig. 3. A detailed examination
 441 reveals a close resemblance to CSH₁. This behavior is expected, as in our samples the ratio of Al
 442 ions per Si is 0.1, and the effect of the Al is limited. However, some differences should be
 443 addressed.

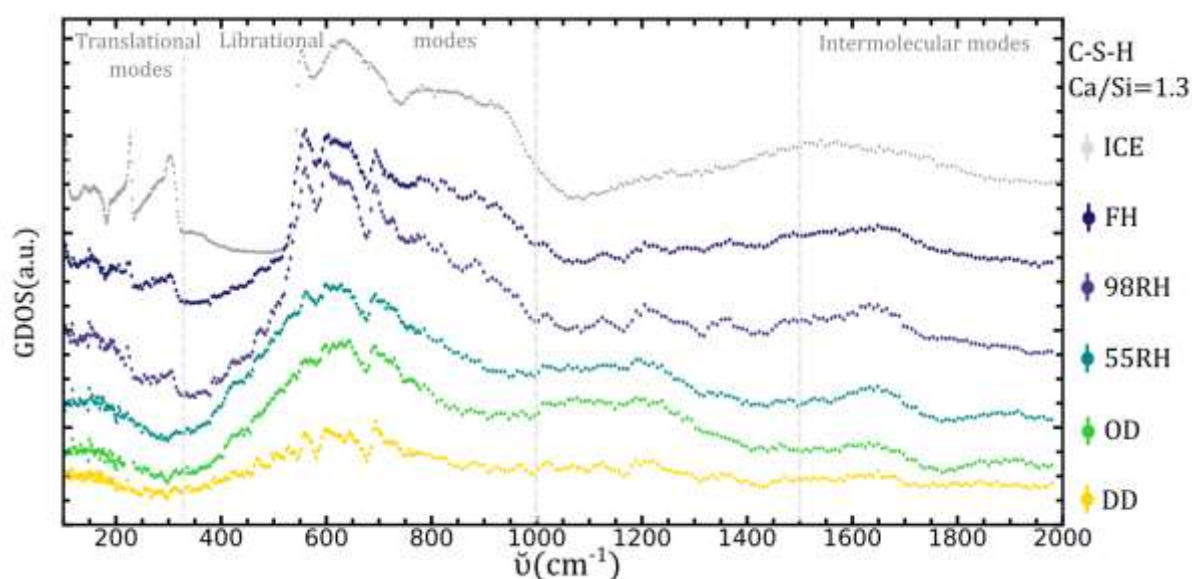
444 First, similar to the CSH_1_98RH, the CASH_0.9_98RH contains multilayer water and some bulk
445 pore water, as deduced from the librational edge, which could be decomposed as a linear
446 combination of the signals from CASH_0.9_55H, and ice Ih edges. However, the relative intensities
447 of the lower energy range translational modes (100-250 cm^{-1} , 15-40 meV) to the intensities of the
448 librational modes are closer to those of ice Ih, than in CSH_1. This can be explained by the greater
449 amount of water adsorbed at a given RH for CASH_0.9 than for the CSH_1 samples as shown by
450 the results of WSI, TGA, and XRD (Table 1).

451 Secondly, the shape of CASH_0.9_98RH coincides with the shape of Ice Ih (Fig. 2.B), except for the
452 absence of the characteristic dip in intensity at 350-550 cm^{-1} (43.4-68 meV) and the lower
453 intensities of the acoustic mode at 56.5 cm^{-1} (7 meV). This reveals that multilayer water
454 adsorption leads to capillary condensation of water in the larger gel pores and capillary pores
455 with increasing RH. Another difference is in the acoustic mode peak which was damped and
456 shifted in CSH_1 and is wider in the case of CASH_0.9, in line with our discussion about the
457 changing value, shape, and intensity of this band.

458 **4.2.3 Impact of RH level in CSH_1.3**

459 The evolution of spectra for C-S-H with Ca/Si = 1.3 (CSH_1.3) as a function of RH is shown in Fig.
460 4. The tendency towards the formation of an ice-like structure at increasing RH values is again
461 observed. However, there are a few significant differences, which stem from the changing nature
462 of C-S-H depending on the Ca/Si ratio.

463



464

465 *Fig. 4. Evolution of the GDOS of CSH_1.3 samples with increasing hydration state. All the spectra have been*
466 *normalized to the water content of the sample in the beam. For the sake of clarity, all the spectra have been*
467 *arbitrarily shifted along the GDOS axis. The translations of water molecules at 226 and 305 cm^{-1} (28 and 38*
468 *meV) evident in samples containing bulk-like water (98RH) evolve into dampened signals upon loss of water.*

469 *Additionally, the OV sample shows a peak at 260 cm⁻¹ (32 meV). Similar to CSH_1 and CSH_1.3 samples, the*
470 *librational edges evolve from the sharp vertical onset in the ice into a rising slope in dry samples (55RH, OD,*
471 *DD). The librational edges of FH and 98RH samples contain features of both bulk-like water and interfacial*
472 *and interlayer water. The librational modes in the 55RH sample, which are indicative of the hydrogen bonding*
473 *network, alter their shape and intensity as they transition from an ice-like distribution to a broader triangular*
474 *distribution. This transition occurs in a frequency range from 400 to 1000 cm⁻¹ (corresponding to 50 to 125*
475 *meV). These sets of spectra have been collected at IN1-Lagrange, ILL. The x-axis starts from 100 cm⁻¹ due to*
476 *the experimental setup.*

477 The main differences are observed in the range of low energies for CSH_1.3 compared to CSH_1
478 and CASH_0.9. The very different shape of spectra at lower energies comes from the peculiarities
479 of the IN1-Lagrange instrument where the data were collected. The Q range for CSH_1.3 samples
480 spans from 100-2000 cm⁻¹ (~15-250 meV), which is obtained by stitching the IN1-Lagrange data
481 from the two monochromators manually. The acoustic signals at 226 and 298 cm⁻¹ (28 and 37
482 meV) present in ice Ih exist also in CSH_1.3_FH, and with lesser intensities in CSH_1.3_98RH
483 samples.

484 The 'wet' CSH_1.3 samples show fewer ice-like features than C-S-H_1 samples for a given RH. We
485 also performed a linear combination fitting for the CSH_1.3_98RH sample and found a good fit
486 with 60% of dFH and 40% of d55RH samples (Fig. 3.B), comparable to the TGA data. The TGA
487 data shows that water adsorbed upon rewetting of CSH_1.3 sample at 98% RH consists of 38%
488 bulk-liquid-like water, which evaporates at 114°C, and of 62% multilayer adsorbed water.

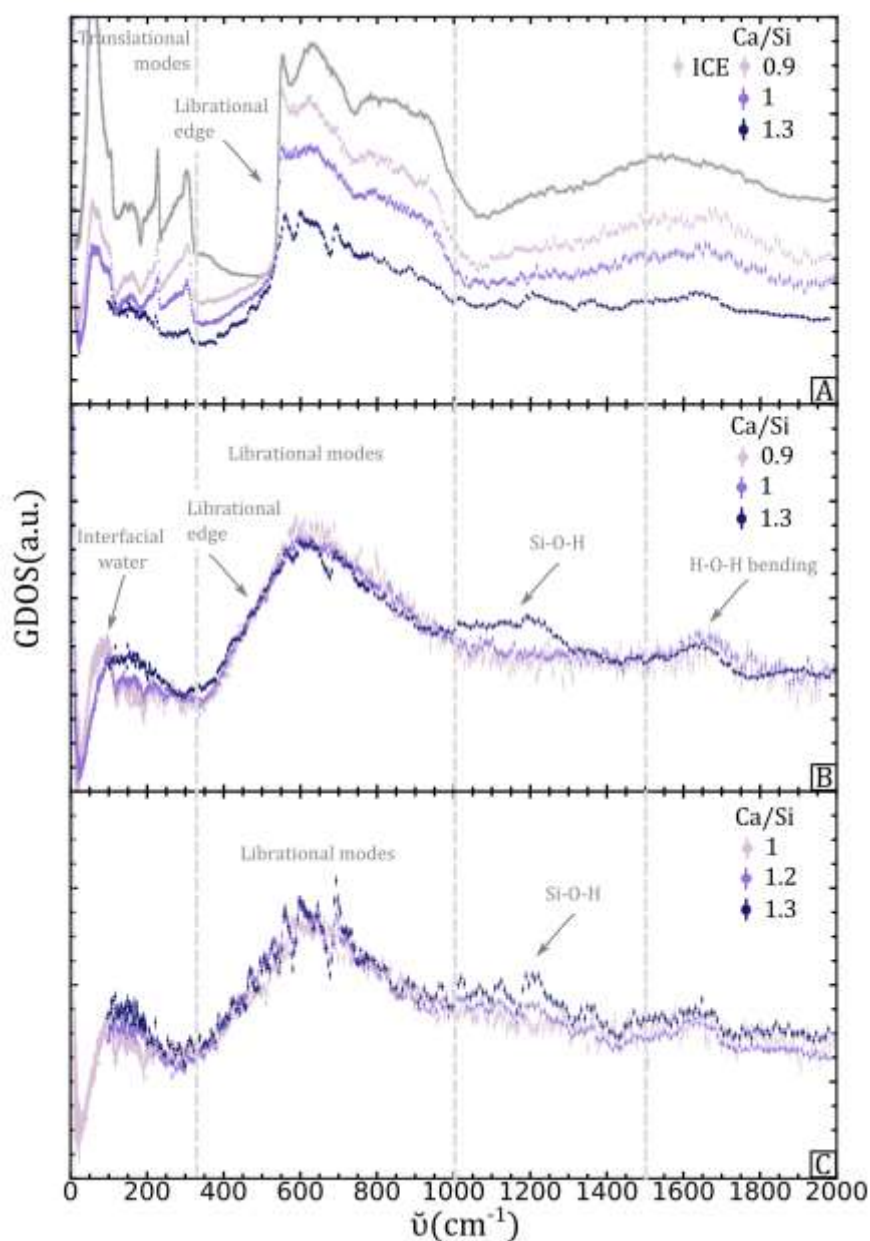
489 The difference between CSH_1, CASH_0.9, and CSH_1.3 samples can be explained based on three
490 factors: (i) C-S-H samples tend to adsorb less water at a given RH with increasing Ca/Si ratios.
491 This observation is supported by the results of WSI, which show that the amount of adsorbed
492 water at 98% RH is 1.1 times higher for CASH_0.9 than for CSH_1 and 1.6 times higher than for
493 CSH_1.3 (Table 1). (ii) A high number of Ca²⁺ sites in the sample implies a higher proportion of
494 Ca-hydration water, which is highly structured (i.e., non-bulk water). Our MD simulations, as well
495 as others [88], showed that Ca²⁺ ions act as hydrophilic centers creating hydration shells and
496 induce a H-bonding network. Therefore, a higher density of calcium ions in CSH_1.3 results in a
497 greater proportion of bound water and a smaller proportion of bulk-liquid-like water. (iii) We
498 note that the amount of adsorbed water on C-(A)-S-H surfaces is highly dependent on the
499 equilibration time [89,90]. In our case, the CASH_0.9 sample was equilibrated under 98% RH
500 conditions 4 times longer than the C-S-H samples (1 month vs. 1 week). Therefore, the larger
501 amount of adsorbed water can be explained partially by a lengthier exposure to a high humidity
502 atmosphere.

503 Overall, the shapes of the librational modes can be used to differentiate between adsorbed
504 interfacial water and bulk pore ice-like water in all C-(A)-S-H samples. For all C-(A)-S-H samples
505 equilibrated at higher RH levels we observed a very close resemblance to ice Ih due to the

506 presence of bulk-liquid-like pore water, whereas at lower RH levels typical confined water signals
507 were present at lower energies of confined water were present in CSH_1 and CASH_0.9 samples.

508 ***4.2.4 Amount and distribution of water as a function of Ca/Si ratio***

509 In Fig. 5, we highlight differences in the IINS spectra arising from changing Ca/Si ratio in 'wet and
510 'dry' C-(A)-S-H samples. We note that we simultaneously examine the *amount* and *distribution* of
511 adsorbed water since IINS allows observing directly both of these characteristics. There is a direct
512 dependence between an increased amount of water and an enhanced spectral intensity. At the
513 same time, the type of water affects the overall shape (and to some extent the intensity) of the
514 spectra. The two types of water that IINS allows us to distinguish are interfacial and interlayer
515 water versus bulk-liquid-like water.



516
 517 *Fig. 5. Experimental generalized density of states for C-(A)-S-H samples with varying RH levels and Ca/Si*
 518 *ratios. (A) 98RH samples show less ice-like features and more structured water increasing Ca/Si*
 519 *ratios. Librational edges at higher Ca/Si ratios reflect a greater abundance of interfacial and interlayer water and a*
 520 *smaller abundance of bulk-liquid-like capillary water; (B) In 55RH samples, an interfacial water signal at 96*
 521 *cm⁻¹ (12 meV) is observed, which is proportional to the amount of adsorbed interfacial water. Samples with*
 522 *lower Ca/Si ratios tend to exhibit slightly higher intensities for this peak. (C) DD samples show an increasing*
 523 *Si-O-H signal with increasing Ca/Si ratio.*

524 The 'wet' FH C-S-H samples show a steep decrease in the amount of adsorbed water at increasing
 525 Ca/Si ratios as witnessed from both TGA and WSI experiments. The 'dry' C-S-H samples show a
 526 smaller difference in the amount of adsorbed water at rising Ca/Si ratios as seen by the amount
 527 of water in 55% RH samples from TGA and WSI (Table 1). These trends correlate well with the
 528 IINS data, where in the case of 98RH samples we can follow the increasing amounts of adsorbed
 529 water with decreasing Ca/Si ratios (Fig. 5.A).

530 However, the conditioning protocol (Fig. S.1 in the Supporting Information) has an effect on the
531 total amount of adsorbed water as a function of Ca/Si (Table 1). As noted earlier, the equilibration
532 time is an important factor when the adsorption of water in C-(A)-S-H is discussed [89]. As
533 Badmann et al. (1981) noted in their work, at RH levels > 95% RH adsorption is superimposed by
534 capillary condensation, therefore the adsorbed volume is more a function of time than humidity
535 [76]. The longer exposure to a higher RH atmosphere of CASH_0.9 could have affected the amount
536 of water adsorbed compared to CSH_1 and CSH_1.3.

537 The same logic can be applied to the 55RH samples (Fig. 5.B), where the relative decrease in area
538 is less apparent than for 98RH samples. The CASH_0.9_55RH sample contains about 1.9 times
539 more adsorbed water than CSH_1 and CSH_1.3 samples. This property of C-(A)-S-H to adsorb less
540 water at higher Ca/Si ratios can be explained by the decreasing surface area shown in Table 1.
541 Gaboreau et al. (2020) showed with XRD analysis that the stacking of the C-S-H layers increased
542 from 3-6 to about 8 as the ratio of Ca/Si increases from 1 to 1.2 [7]. The authors also observed a
543 decreasing SSA calculated from WSI data with rising Ca/Si ratio [7,8], albeit acknowledging that
544 effects such as interstratification (stacking of structurally different layers along c^* axis) and
545 turbostratic stacking (random rotations of layers) could affect the results [91].

546 Based on the above discussion, we argue that the amount of adsorbed water is a delicate balance
547 between the equilibration time and available surface area. On the other hand, the distribution of
548 the adsorbed water is most probably affected by an increased number of Ca^{2+} ions, not only in the
549 interlayers but also on the surfaces of C-(A)-S-H. These calcium ions form hydrophilic sites for
550 water that are highly structured.

551 Finally, the comparison of DD samples at different Ca/Si ratios (Fig. 5.C) shows that they have
552 matching intensities, except for the region around 1100 cm^{-1} (136.4 meV). This intensity is
553 characteristic of silanol hydroxyl groups as shown for different minerals [53].

554 In summary, we have applied the IINS experiment to probe the dynamics of water in our C-(A)-S-
555 H samples with three Ca/Si ratios (0.9, 1, 1.3) at five hydration levels. The resulting GDOS allows
556 us to distinguish different types of water present in our samples: interfacial and interlayer water
557 strongly affected by C-(A)-S-H surfaces; bulk-liquid-like capillary pore water, resembling ice Ih;
558 and intermediate samples containing both multilayer interfacial and bulk-like water. The method
559 permits the observation of characteristic bands coming from translational movements, bending
560 and stretching motions of water molecules, and most importantly, from librational motions (H-
561 bond hindered translations and rotations of water molecules).

562 **4.3 Computed IINS data**

563 To complement our experimental IINS data, we performed classical MD simulations and
564 calculated the associated generalized density of states (GDOS). Predicted GDOS were calculated
565 for different hydrogen populations reflecting different water distributions in our ‘wet’ and ‘dry’
566 C-(A)-S-H samples. We used two atomistic C-S-H models developed in our previous work [37]: a
567 ‘dry’ atomic model named ‘CSH-dry-NP’ with H₂O/Si ratio of 1.35 and interlayer spacing $d_{001-MD} =$
568 $11.0(2) \text{ \AA}$ and a fully hydrated model ‘CSH-wet-NP’ with H₂O/Si ratio of 38.5 and an interlayer
569 spacing $d_{001-MD} = 13.0(2) \text{ \AA}$. The direct comparison of the GDOS calculated from our MD simulation
570 trajectories with our measured vibrational spectra is consistent with our experimental
571 conclusions. Moreover, water diffusion coefficients calculated for our ‘CSH-dry-NP’ model
572 confirms the presence of the highly bound interfacial/interlayer water in our ‘dry’ C-(A)-S-H
573 samples.

574 **4.3.1 Bulk water vs interfacial and interlayer water**

575 GDOS were calculated for all populations of hydrogen atoms (water and hydroxyl hydrogens) in
576 the ‘CSH-dry-NP’ model and the bulk water (Fig. S.8 in the Supporting Information). The shapes
577 and intensities of the vibrational modes of water of the ‘CSH-dry-NP’ model are very different
578 from the ones of bulk water. Differences are present in all regions of the spectra: at lower
579 frequencies we observe a peak at 260 cm^{-1} ($\sim 32.2 \text{ meV}$), which is not present in bulk water,
580 followed by librational modes having half the intensity of bulk water, and an additional broad
581 peak centered around 1100 cm^{-1} (136.4 meV). The origins of these signals will be addressed later.
582 Intramolecular vibrations are observed at higher frequencies, including the H-O-H bending peak
583 generally expected at around 1600 cm^{-1} (198.4 meV) and the O-H stretching signal at around 3600
584 cm^{-1} (446.3 meV).

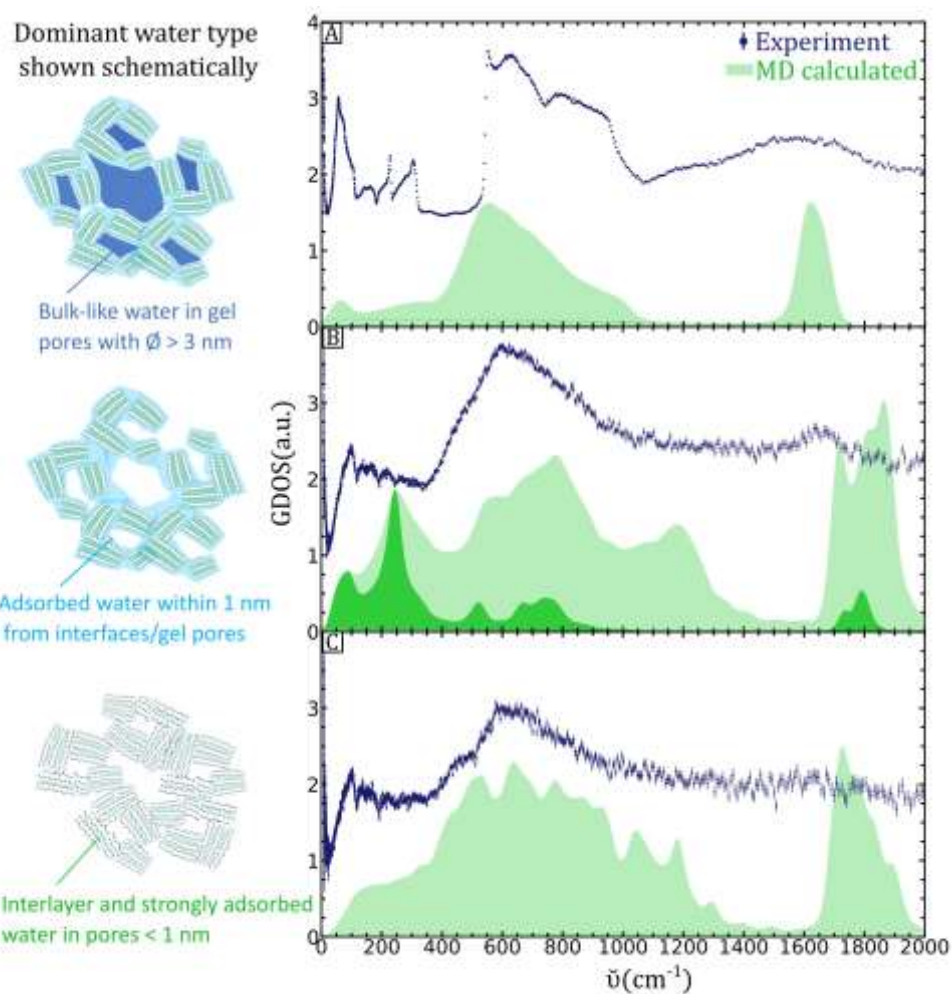
585 The bending peak for the calculated bulk water is centered at the expected value 1650 cm^{-1} ,
586 whilst the bending in CSH_1_55RH is split into two, occurring at about 1725 and 1830 cm^{-1} (213.5
587 meV and 226.5 meV), indicating a clear deviation from the bulk water. The stretching modes for
588 bulk water are centered at 3730 cm^{-1} (462.4 meV) and 3810 cm^{-1} (472.4 meV), and for the ‘CSH-
589 dry-NP’ model at 3677 and 3830 cm^{-1} (455.9 and 474.8 meV). A blue shift for the expected
590 stretching values is most probably due to the limitations of the SPC water model, in addition to
591 the interlayer and interfacial water properties in ‘CSH-dry-NP’.

592 The calculated total GDOS of the ‘CSH-dry-NP’ system consists of contributions from hydrogens
593 of water and hydrogens of structural hydroxyls. Since there are 132 hydroxyl hydrogens and 896
594 water hydrogens in the simulated ‘dry’ system, the total GDOS signal is dominated by the
595 hydrogens of molecular water (Fig. S.9 in the Supporting Information).

596 **4.3.2 Experimental IINS data vs MD calculated GDOS data**

597 Here, we compare the experimental data to our calculated GDOS and evaluate whether the
 598 comparison is consistent with the conclusions made in the experimental section 4.3.1.

599 The GDOS of water hydrogens can be separated depending on the local environment of the H
 600 atoms: (A) water hydrogens in the first hydration shell of calcium ions, and/or forming H-bonds
 601 with the C-S-H surfaces; (B) hydrogens forming hydrogen bonds with other water molecules and;
 602 (C) hydrogens not involved in any kind of bonding (Fig. S.10 in the Supporting Information).
 603 These different types of hydrogens result in IINS signals at different energies as shown in Fig. 6.

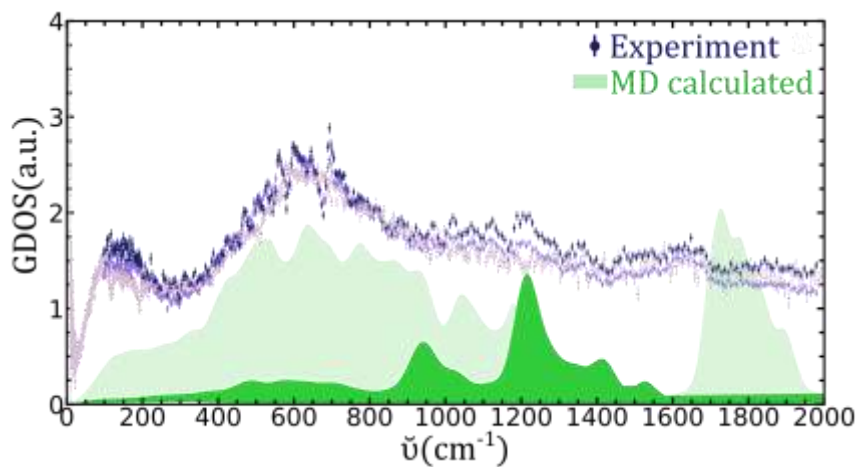


604

605 *Fig. 6. (right) Experimental and calculated GDOS for CSH_1 samples with varying water content (A) FH; (B)*
 606 *55RH; (C) DD; (left) Schematic images of C-(A)-S-H containing different water types: strongly bound interlayer*
 607 *and interfacial water are in green; adsorbed multilayer interfacial water is in light blue; bulk-like capillary*
 608 *pore water are in dark blue. (A) The experimental FH spectrum is dominated by the bulk-like capillary water*
 609 *found in gel pores larger than ~ 3 nm. The MD simulated GDOS reproduces a characteristic peak at 80 cm⁻¹*
 610 *(10 meV) attributed to the translations of water molecules in ice Ih, a sharp librational edge starting at ~ 550*
 611 *cm⁻¹ (68 meV), and the H-O-H bending modes at 1650 cm⁻¹ (206 meV); (B) The experimental 55RH spectrum*
 612 *is dominated by adsorbed interfacial water found on the surfaces of gel pores within about 1 nm from the C-*
 613 *(A)-S-H interfaces. The MD simulated GDOS of total water in CSH_1_55RH nanoparticle model containing*
 614 *interfacial and interlayer water is shown in light green. The MD-generated partial GDOS (shaded dark green)*
 615 *represents interfacial dangling water hydrogen atoms with characteristic signals at 96 cm⁻¹ and 245 cm⁻¹ (12*

616 and 30 meV). H-O-H bending modes in the 55RH sample are at 1650 cm^{-1} in the experimental spectrum, and
617 at 1800 cm^{-1} in MD generated one; (C) The experimental DD spectra is dominated by strongly bound interlayer
618 water in pores smaller than 1 nm, and interfacial water within 1 nm (e.g., 3 water monolayers) from the C-
619 (A)-S-H surfaces. The MD-generated partial GDOS represents interlayers of the CSH_1_55RH nanoparticle
620 model. The absence of the peaks at 96 cm^{-1} and 245 cm^{-1} confirms that they are associated interfacial water.

621 The lower frequency ($<300 \text{ cm}^{-1}$) contributions originate mainly from the dangling water
622 hydrogens and from the water molecules H-bonded to other water molecules, as demonstrated
623 in light blue in Fig. 6. The signal at about 55 cm^{-1} (7 meV) in ice decreases in intensity and
624 broadens for samples containing interfacial and interlayer water. Our calculated GDOS shows
625 these peaks at 80 cm^{-1} (9.9 meV) and 260 cm^{-1} (32.2 meV) come from the dangling interfacial
626 water hydrogens and H-bonded interfacial water molecules. Moreover, when only the interlayer
627 region is selected in the 'CSH-dry-NP' and 'CSH-wet-NP' models, these lower energy signals
628 disappear (Fig. S.11 in the Supporting Information), meaning that there are no dangling water
629 hydrogens in the interlayer region. These dangling interfacial hydrogens are responsible for an
630 extra peak at $\sim 249 \text{ cm}^{-1}$ present only in oven-dried samples (bright green on Fig. 2.A and 2.B).
631 Most probably this peak signifies a monolayer of adsorbed interfacial water (hence dangling
632 hydrogens), which stems from the wetting mechanism of the C-(A)-S-H surfaces as evidenced by
633 our MD simulations.



634

635 *Fig. 7. (Blue and purple symbols) Experimental IINS spectra for DD CSH_1, CSH_1.2, and CSH_1.3; (Shaded light*
636 *green area) Calculated GDOS of interlayer hydrogens show the absence of interfacial hydrogen peaks at 80*
637 *cm^{-1} (9.9 meV) and 260 cm^{-1} (32.2 meV); (Shaded dark green area) Calculated partial GDOS of interlayer*
638 *hydroxyl hydrogen atoms showing intensity to the signal centered at 1100 cm^{-1} .*

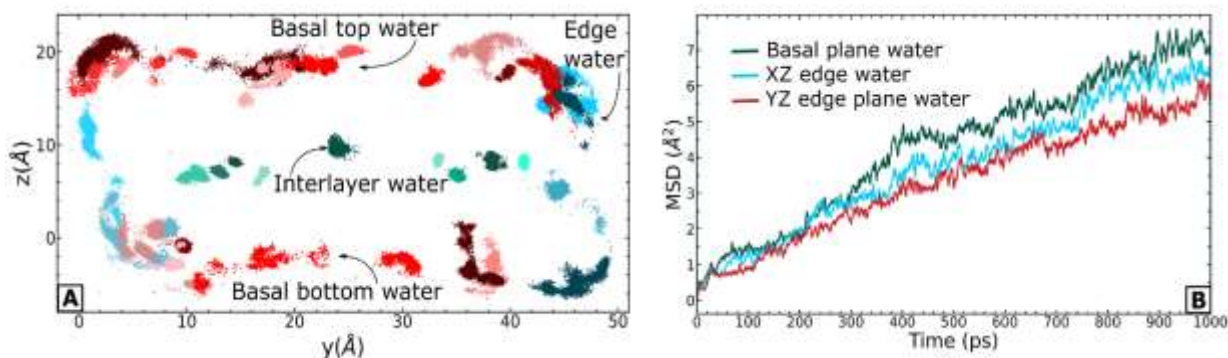
639 We calculated the vibrational density of states for the silanol hydroxyls [53] found in the
640 interlayer that showed the intensity centered at 1100 cm^{-1} (136.4 meV) (Fig. 7). This signal
641 increases with the Ca/Si ratios. Recent findings based on ^1H NMR experiments and theoretical
642 calculations showed similar trends [92]. It is known that at higher Ca/Si ratios the number of
643 defects increases as evidenced by the increased number of Q¹ silicons (Si atoms connected only
644 to another Si atom) and mean length of Si chain (the mean number of silica tetrahedra forming

645 chains)[93]. We found that the 1100 cm^{-1} (from 900 to 1400 cm^{-1}) signal in DD samples increases
646 consistently from CSH_1 to CSH_1.2 to CSH_1.3.

647 These hydroxyl signals do not arise from calcium hydroxide-like species. We have verified the
648 absence of portlandite by comparing the IINS spectra of portlandite ($\text{Ca}(\text{OH})_2$) with our C-(A)-S-
649 H spectra. Portlandite generally shows an intense peak at 330 cm^{-1} (41 meV) and is clearly visible
650 in INS spectra of cement pastes with higher Ca/Si ratios ($\text{Ca/Si} > 1.6$ [18]). Although it remains
651 difficult to assign these signals definitively to the silanol hydroxyls as previous literature points
652 to the opposite trends of the number of Si-OH decreasing with increasing Ca/Si ratios [5,94].
653 Careful analysis of our results suggests that silanol hydroxyl groups in C-(A)-S-H show increased
654 signal intensity at higher Ca/Si due to an increased number of defects at higher Ca/Si ratios.

655 4.3.3 Diffusion of water in 'CSH-dry-NP'

656 The trajectories of oxygen atoms of water were followed over 5 ns , revealing a very restricted
657 motion over the course of the production run (Fig. 8.A). The mean square displacement (MSD) of
658 water molecules in the 'CSH-dry-NP' system (Fig. 8.B) has been used to calculate the self-diffusion
659 coefficient of interfacial water. The obtained value of $6.8 \times 10^{-11}\text{ m}^2/\text{s}$ compares well to other
660 reported values (from 2.6 to $5 \times 10^{-11}\text{ m}^2/\text{s}$) for interfacial/confined water in C-S-H [30].



661

662 *Fig. 8. (A) The trajectories of water oxygens followed for 5 ns shown in the YZ plane for 'CSH-dry-NP'; (B) The*
663 *MSD of water molecules on the 'CSH-dry-NP' interfaces during 1 ns.*

664 5 CONCLUSIONS

665 Inelastic Incoherent Neutrons Scattering experiment, complemented with MD simulations, WSI,
666 and TGA data, is a powerful approach to probe the vibrational dynamics of water in confined
667 systems such as C-(A)-S-H surfaces and pores. The spectra exhibit a range of features that allow
668 attributing different properties to the water in the different regions of the samples. Our combined
669 approach shows that at lower energies ($<300\text{ cm}^{-1}$ or 37.2 meV) the so-called 'fingerprint' signal
670 of confined water at around 80 cm^{-1} (9.9 meV) was present in the 'dry' C-(A)-S-H samples, with
671 the oven-dried samples showing a peak at 260 cm^{-1} (32.2 meV) possibly belonging to a thin

672 monolayer of interfacial water. At intermediate energies, the shape of the librational region is
673 different for water confined at interfaces, showing a broadband that starts at $\sim 300\text{ cm}^{-1}$ (37.2
674 meV), as opposed to 550 cm^{-1} (68.2 meV) for bulk-like water. A linear combination fitting was
675 applied to fit 98RH samples as a mixture of multilayer adsorbed and bulk-liquid-like water. The
676 high energy ($>1000\text{ cm}^{-1}$ or 124 meV) intramolecular bending and stretching modes are present
677 in the experimental data but with significantly dampened intensities. The calculated GDOS
678 reproduced these intramolecular vibrations, albeit blue-shifted due to the nature of confined
679 water in our dry samples, and approximations associated with the SPC water model.

680 Differences in both the amount and the distribution of adsorbed water were found when
681 increasing the Ca/Si ratio. At 98% RH, CSH_1.3 samples adsorbed significantly less water than
682 CSH_1, which in turn adsorbed less water than CASH_0.9. The water at higher Ca/Si ratios was
683 also more structured, i.e., less bulk-liquid-like. This observation can be rationalized by
684 considering the number of adsorption sites for water present in the different samples. At high
685 Ca/Si ratios, more Ca^{2+} is present in the samples. This cation acts as a strong center of charge,
686 very hydrophilic in nature, thus creating more adsorption sites for water. This water is not only
687 bonded to the Ca^{2+} cation, but it also forms hydrogen bonds with oxygen atoms from the structure.

688 Confined, strongly bound, water from the first coordination sphere of Ca^{2+} has limited diffusivity
689 and forms strong hydrogen bonds with surface oxygen atoms, in particular in the interlayer
690 region. Previous studies have reported an increase of the stacking along the \mathbf{c}^* direction upon the
691 increase of the Ca/Si ratio in the samples. This increased stacking could lead to an eventual higher
692 crystallinity, with better-defined sites for water adsorption (water from the Ca^{2+} hydration shell).

693 Overall, our experimental and simulation results converge towards a picture where the evolution
694 from thin layers of adsorbed water to bulk capillary water is dampened by the structure of C-(A)-
695 S-H, in particular by the availability of Ca^{2+} sites that tend to keep the water in the form of
696 structured surface layers.

697 Determining the range of humidity at which bulk-like water is present in C-(A)-S-H samples is of
698 major importance to understand better some of the mechanisms that take present or controlled
699 by the properties of C-(A)-S-H – water interfaces. This is the case, for instance, of the carbonation
700 reaction that takes place in the presence of dissolved CO_2 . As in a saturated system, the presence
701 of capillary water tends to lead to dissolution–reprecipitation processes, unlike the solid-state
702 transformation that takes place under non-saturated conditions [95]. It is expected that other
703 processes, such as creep, can be influenced by the presence of adsorbed vs. bulk-like water [96].

704 **6 ACKNOWLEDGEMENTS**

705 Use of the Geochemistry-Mineralogy platform at ISTERre is acknowledged. A.F.-M. and A.E.S.V.-D.
706 acknowledge funding from the ANR-JCJC 'NUANCE' project (grant ANR-17-CE08-0057). We thank
707 the IDEX mobility scholarship program of the University of Grenoble-Alpes for supporting a
708 research stay at Princeton University. We thank the Institut Laue-Langevin, ISIS Neutron and
709 Muon Source, and European Synchrotron Radiation Facility for allocated beamtimes. I.C.B. was
710 supported by the U.S. Department of Energy, Office of Science, Office of Basic Energy Sciences,
711 Geosciences Program under Award DE-SC0018419. Molecular dynamics simulations were
712 performed using resources of the National Energy Research Scientific Computing Center
713 (NERSC), which is supported by the U.S. Department of Energy, Office of Science, under Award
714 DE-AC02-05CH11231. Z.Z. thanks BRGM for cofounding her PhD, Dr. Arianna d'Angelo for fruitful
715 discussions about DOS calculations, and Prof. John L. Provis for the deep insights about C-A-S-H.

716 **REFERENCES:**

- 717 [1] G. Goracci, M. Monasterio, H. Jansson, S. Cervený, Dynamics of nano-confined water in
718 Portland cement - comparison with synthetic C-S-H gel and other silicate materials., *Sci.*
719 *Rep.* 7 (2017) 8258. <https://doi.org/10.1038/s41598-017-08645-z>.
- 720 [2] M. Vandamme, F.-J. Ulm, Nanogranular origin of concrete creep, *Proc. Natl. Acad. Sci.* 106
721 (2009) 10552–10557. <https://doi.org/https://doi.org/10.1073/pnas.0901033106>.
- 722 [3] H.N. Bordallo, L.P. Aldridge, A. Desmedt, Water dynamics in hardened ordinary Portland
723 cement paste or concrete: from quasielastic neutron scattering, *J. Phys. Chem. B.* 110
724 (2006) 17966–17976. <https://doi.org/10.1021/jp062922f>.
- 725 [4] M.B. Pinson, E. Masoero, P.A. Bonnaud, J.J. Thomas, M.Z. Bazant, Hysteresis from
726 multiscale porosity : modeling water sorption and shrinkage in cement paste, *Phys. Rev.*
727 *Appl.* 3 (2015) 064009–066016.
728 <https://doi.org/https://doi.org/10.1103/PhysRevApplied.3.064009>.
- 729 [5] I.G. Richardson, Tobermorite/jennite- and tobermorite/calcium hydroxide-based models
730 for the structure of C-S-H: Applicability to hardened pastes of tricalcium silicate, β -
731 dicalcium silicate, Portland cement, and blends of Portland cement with blast-furnace
732 slag, metakaol, *Cem. Concr. Res.* 34 (2004) 1733–1777.
733 <https://doi.org/https://doi.org/10.1016/j.cemconres.2004.05.034>.
- 734 [6] A. Valori, P.J. McDonald, K.L. Scrivener, The morphology of C-S-H: Lessons from 1H
735 nuclear magnetic resonance relaxometry, *Cem. Concr. Res.* 49 (2013) 65–81.
736 <https://doi.org/https://doi.org/10.1016/j.cemconres.2013.03.011>.

- 737 [7] S. Gaboreau, S. Grangeon, F. Claret, D. Ihiawakrim, O. Ersen, V. Montouillout, N. Maubec, C.
738 Roosz, P. Henocq, C. Carteret, Hydration Properties and Interlayer Organization in
739 Synthetic C-S-H, *Langmuir*. 36 (2020) 9449–9464.
740 <https://doi.org/https://doi.org/10.1021/acs.langmuir.0c01335>.
- 741 [8] C. Roosz, S. Gaboreau, S. Grangeon, D. Prêt, V. Montouillout, N. Maubec, S. Ory, P. Blanc, P.
742 Vieillard, P. Henocq, Distribution of water in synthetic calcium silicate hydrates,
743 *Langmuir*. 32 (2016) 6794–6805.
744 <https://doi.org/https://doi.org/10.1021/acs.langmuir.6b00878>.
- 745 [9] P.J. McDonald, V. Rodin, A. Valori, Characterisation of intra- and inter-C–S–H gel pore
746 water in white cement based on an analysis of NMR signal amplitudes as a function of
747 water content, *Cem. Concr. Res.* 40 (2010) 1656–1663.
748 <https://doi.org/https://doi.org/10.1016/j.cemconres.2010.08.003>.
- 749 [10] P.J. McDonald, J.-P. Korb, J. Mitchell, L. Monteilhet, Surface relaxation and chemical
750 exchange in hydrating cement pastes: A two-dimensional NMR relaxation study, *Phys.*
751 *Rev. E.* 72 (2005) 11409. <https://doi.org/10.1103/PhysRevE.72.011409>.
- 752 [11] Z. Hu, M. Wyrzykowski, K. Scrivener, P. Lura, A novel method to predict internal relative
753 humidity in cementitious materials by ^1H NMR, *Cem. Concr. Res.* (2017) 1–14.
754 <https://doi.org/10.1016/j.cemconres.2017.11.001>.
- 755 [12] F. Barberon, J.P. Korb, D. Petit, V. Morin, E. Bermejo, Probing the Surface Area of a
756 Cement-Based Material by Nuclear Magnetic Relaxation Dispersion, *Phys. Rev. Lett.* 90
757 (2003) 4. <https://doi.org/10.1103/PhysRevLett.90.116103>.
- 758 [13] L. Monteilhet, J.-P. Korb, J. Mitchell, P.J. McDonald, Observation of exchange of micropore
759 water in cement pastes by two-dimensional $T(2)$ - $T(2)$ nuclear magnetic resonance
760 relaxometry., *Phys. Rev. E. Stat. Nonlin. Soft Matter Phys.* 74 (2006) 61404.
761 <https://doi.org/10.1103/PhysRevE.74.061404>.
- 762 [14] R. Blinc, M. Burgar, G. Lahajnar, M. Rozmarin, V. Rutar, I. Kocuvan, J. Ursic, NMR
763 Relaxation Study of Adsorbed Water in Cement and C3S Pastes, *J. Am. Ceram. Soc.* 61
764 (1978) 35–37. <https://doi.org/https://doi.org/10.1111/j.1151-2916.1978.tb09224.x>.
- 765 [15] F. Ridi, E. Fratini, S. Milani, P. Baglioni, Near-Infrared Spectroscopy Investigation of the
766 Water Confined in Tricalcium Silicate Pastes, *J. Phys. Chem. B.* 110 (2006) 16326–16331.
767 <https://doi.org/10.1021/jp060026y>.
- 768 [16] S. Cerveny, S. Arrese-Igor, J.S. Dolado, J.J. Gaitero, A. Alegra, J. Colmenero, Effect of

- 769 hydration on the dielectric properties of C-S-H gel, *J. Chem. Phys.* 134 (2011).
770 <https://doi.org/10.1063/1.3521481>.
- 771 [17] S.A. FitzGerald, D.A. Neumann, J.J. Rush, R.J. Kirkpatrick, X. Cong, R.A. Livingston, Inelastic
772 neutron scattering study of the hydration of tricalcium silicate, *J. Mater. Res.* 14 (1999)
773 1160–1165. [https://doi.org/DOI: 10.1557/JMR.1999.0154](https://doi.org/DOI:10.1557/JMR.1999.0154).
- 774 [18] J.J. Thomas, J.J. Chen, H.M. Jennings, D.A. Neumann, Ca-OH bonding in the C-S-H gel phase
775 of tricalcium silicate and white portland cement pastes measured by inelastic neutron
776 scattering, *Chem. Mater.* 15 (2003) 3813–3817. <https://doi.org/10.1021/cm034227f>.
- 777 [19] N.M. Nemes, D.A. Neumann, R.A. Livingston, States of water in hydrated C3S (tricalcium
778 silicate) as a function of relative humidity, *J. Mater. Res.* 21 (2006) 2516–2523.
779 <https://doi.org/https://doi.org/10.1557/jmr.2006.0332>.
- 780 [20] R. Livingston, D. Neumann, A. Allen, J. Rush, Application of Neutron Scattering Methods to
781 Cementitious Materials, *MRS Proc.* 376 (1994) 459.
782 <https://doi.org/https://doi.org/10.1557/PROC-376-459>.
- 783 [21] K. Amann-Winkel, M.-C. Bellissent-Funel, L.E. Bove, T. Loerting, A. Nilsson, A. Paciaroni, D.
784 Schlesinger, L. Skinner, X-ray and Neutron Scattering of Water, *Chem. Rev.* 116 (2016)
785 7570–7589. <https://doi.org/10.1021/acs.chemrev.5b00663>.
- 786 [22] M.-C. Bellissent-Funel, S.H. Chen, J.-M. Zanotti, Single-particle dynamics of water
787 molecules in confined space, *Phys. Rev. E.* 51 (1995) 4558–4569.
788 <https://doi.org/10.1103/PhysRevE.51.4558>.
- 789 [23] M.C. Berg, K.N. Dalby, N. Tsapatsaris, D. V. Okhrimenko, H.O. Sørensen, D. Jha, J.P. Embs,
790 S.L.S. Stipp, H.N. Bordallo, Water Mobility in Chalk: A Quasielastic Neutron Scattering
791 Study, *J. Phys. Chem. C.* 121 (2017) 14088–14095.
792 <https://doi.org/10.1021/acs.jpcc.7b01998>.
- 793 [24] V. Crupi, D. Majolino, P. Migliardo, V. Venuti, M.-C. Bellissent-Funel, Structure and
794 dynamics of water confined in a nanoporous sol-gel silica glass: A neutron scattering
795 study, *Mol. Phys.* 101 (2003) 3323–3333.
796 <https://doi.org/10.1080/00268970310001638790>.
- 797 [25] K.W.B. Hunvik, P. Loch, L.P. Cavalcanti, K.K. Seljelid, P.M. Røren, S. Rudić, D. Wallacher, A.
798 Kirch, K.D. Knudsen, C. Rodrigues Miranda, J. Breu, H.N. Bordallo, J.O. Fossum, CO₂
799 Capture by Nickel Hydroxide Interstratified in the Nanolayered Space of a Synthetic Clay
800 Mineral, *J. Phys. Chem. C.* 124 (2020) 26222–26231.

- 801 <https://doi.org/10.1021/acs.jpcc.0c07206>.
- 802 [26] A. Faraone, E. Fratini, P. Baglioni, S.H. Chen, Quasielastic and inelastic neutron scattering
803 on hydrated calcium silicate pastes, *J. Chem. Phys.* 121 (2004) 3212–3220.
804 <https://doi.org/10.1063/1.1772755>.
- 805 [27] M.-C. Bellissent-Funel, S.H. Chen, J.M. Zanotti, Single-particle dynamics of water molecules
806 in confined space, *Phys. Rev. E.* 51 (1995) 4558–4569.
807 <https://doi.org/10.1103/physreve.51.4558>.
- 808 [28] M. Abdolhosseini Qomi, K.J. Krakowiak, M. Bauchy, K.L. Stewart, R. Shahsavari, D.
809 Jagannathan, D.B. Brommer, A. Baronnet, M.J. Buehler, S. Yip, F.-J. Ulm, K.J. Van Vliet, R.-.
810 M. Pellenq, Combinatorial molecular optimization of cement hydrates, *Nat. Commun.* 5
811 (2014) 4960. <https://doi.org/https://doi.org/10.1038/ncomms5960>.
- 812 [29] M. Youssef, R.J.M. Pellenq, B. Yildiz, Glassy nature of water in an ultraconfining
813 disordered material: The case of calcium-silicate-hydrate, *J. Am. Chem. Soc.* 133 (2011)
814 2499–2510. <https://doi.org/https://doi.org/10.1021/ja107003a>.
- 815 [30] M.J. Abdolhosseini Qomi, L. Brochard, T. Honorio, I. Maruyama, M. Vandamme, Advances
816 in atomistic modeling and understanding of drying shrinkage in cementitious materials,
817 *Cem. Concr. Res.* 148 (2021) 106536.
818 <https://doi.org/10.1016/j.cemconres.2021.106536>.
- 819 [31] A.G. Kalinichev, J. Wang, R.J. Kirkpatrick, Molecular dynamics modeling of the structure,
820 dynamics and energetics of mineral-water interfaces: Application to cement materials,
821 *Cem. Concr. Res.* 37 (2007) 337–347.
822 <https://doi.org/https://doi.org/10.1016/j.cemconres.2006.07.004>.
- 823 [32] H.F.W. Taylor, Proposed structure for calcium silicate hydrate gel, *J. Am. Ceram. Soc.* 69
824 (1986) 464–467. <https://doi.org/10.1111/j.1151-2916.1986.tb07446.x>.
- 825 [33] J.-P. Korb, M. Whaley Hodges, R. Bryant, Translational diffusion of liquids at surface of
826 microporous materials: new theoretical analysis of field cycling magnetic relaxation
827 measurements, *Magn. Reson. Imaging.* 16 (1998) 575–578.
828 [https://doi.org/https://doi.org/10.1016/S0730-725X\(98\)00051-4](https://doi.org/https://doi.org/10.1016/S0730-725X(98)00051-4).
- 829 [34] K. Kupwade-Patil, A. Bumajdad, C.M. Brown, M. Tyagi, N.P. Butch, A.F. Jamsheer, O.
830 Büyüköztürk, New insights into water dynamics of Portland cement paste with nano-
831 additives using quasielastic neutron scattering, *J. Mater. Sci.* 54 (2019) 4710–4718.
832 <https://doi.org/10.1007/s10853-018-03212-x>.

- 833 [35] P. Le, E. Fratini, K. Ito, Z. Wang, E. Mamontov, P. Baglioni, S.-H. Chen, Dynamical behaviors
834 of structural, constrained and free water in calcium- and magnesium-silicate-hydrate
835 gels, *J. Colloid Interface Sci.* 469 (2016) 157–163.
836 <https://doi.org/https://doi.org/10.1016/j.jcis.2016.01.071>.
- 837 [36] H.N. Bordallo, L.P. Aldridge, G.J. Churchman, W.P. Gates, M.T.F. Telling, K. Kiefer, P.
838 Fouquet, T. Seydel, S.A.J. Kimber, Quasi-elastic neutron scattering studies on clay
839 interlayer-space highlighting the effect of the cation in confined water dynamics, *J. Phys.*
840 *Chem. C.* 112 (2008) 13982–13991. <https://doi.org/10.1021/jp803274j>.
- 841 [37] Z. Zhakiyeva, G.J. Cuello, H.E. Fischer, D.T. Bowron, C. Dejoie, V. Magnin, S. Campillo, S.
842 Bureau, A. Poulain, R. Besselink, S. Gaboreau, S. Grangeon, F. Claret, I.C. Bourg, A.E.S. Van
843 Driessche, A. Fernandez-Martinez, Structure of water adsorbed on nanocrystalline
844 calcium silicate hydrate determined from neutron scattering and molecular dynamics
845 simulations, *J. Phys. Chem. C.* 126 (2022) 12820–12835.
846 <https://doi.org/https://doi.org/10.1021/acs.jpcc.2c02626>.
- 847 [38] J. Haas, A. Nonat, From C-S-H to C-A-S-H: Experimental study and thermodynamic
848 modelling, *Cem. Concr. Res.* 68 (2015) 124–138.
849 <https://doi.org/https://doi.org/10.1016/j.cemconres.2014.10.020>.
- 850 [39] C. Roosz, P. Vieillard, P. Blanc, S. Gaboreau, H. Gailhanou, D. Braithwaite, V. Montouillout,
851 R. Denoyel, P. Henocq, B. Madé, Thermodynamic properties of C-S-H, C-A-S-H and M-S-H
852 phases: Results from direct measurements and predictive modelling, *Appl. Geochemistry.*
853 92 (2018) 140–156. <https://doi.org/https://doi.org/10.1016/j.apgeochem.2018.03.004>.
- 854 [40] R.F. Feldman, P.J. Sereda, A new model for hydrated Portland cement and its practical
855 implications, *Eng. J.* 53 (1970) 53–59.
856 <https://citeseerx.ist.psu.edu/document?repid=rep1&type=pdf&doi=04e763def1382354ede175cb0356ed47a065301f>.
- 858 [41] S. Brunauer, P.H. Emmett, E. Teller, Adsorption of Gases in Multimolecular Layers, *J. Am.*
859 *Chem. Soc.* 60 (1938) 309–319. <https://doi.org/https://doi.org/10.1021/ja01269a023>.
- 860 [42] J. Kieffer, J.P. Wright, PyFAI: a Python library for high performance azimuthal integration
861 on GPU, *Powder Diffr.* 28 (2013) S339–S350.
862 <https://doi.org/https://doi.org/10.1017/S0885715613000924>.
- 863 [43] B.H. Toby, R.B. Von Dreele, GSAS-II : the genesis of a modern open-source all purpose
864 crystallography software package, 46 (2013) 544–549.
865 <https://doi.org/https://doi.org/10.1107/S0021889813003531>.

- 866 [44] M. Jiménez-Ruiz, A. Ivanov, S. Fuard, LAGRANGE - The new neutron vibrational
867 spectrometer at the ILL, *J. Phys. Conf. Ser.* 549 (2014). [https://doi.org/10.1088/1742-](https://doi.org/10.1088/1742-6596/549/1/012004)
868 [6596/549/1/012004](https://doi.org/10.1088/1742-6596/549/1/012004).
- 869 [45] A. Ivanov, M. Jimenéz-Ruiz, J. Kulda, IN1-Lagrange-the new ILL instrument to explore
870 vibration dynamics of complex materials, *J. Phys. Conf. Ser.* 554 (2014) 1–7.
871 <https://doi.org/10.1088/1742-6596/554/1/012001>.
- 872 [46] D. Richard, M. Ferrand, G.J. Kearley, Analysis and Visualisation of Neutron-Scattering
873 Data, *J. Neutron Res.* 4 (1996) 33–39. <https://doi.org/10.1080/10238169608200065>.
- 874 [47] S.F. Parker, F. Fernandez-Alonso, A.J. Ramirez-Cuesta, J. Tomkinson, S. Rudic, R.S. Pinna,
875 G. Gorini, J. Fernández Castañon, Recent and future developments on TOSCA at ISIS, *J.*
876 *Phys. Conf. Ser.* 554 (2014). <https://doi.org/10.1088/1742-6596/554/1/012003>.
- 877 [48] R.S. Pinna, S. Rudić, S.F. Parker, J. Armstrong, M. Zanetti, G. Škoro, S.P. Waller, D. Zacek,
878 C.A. Smith, M.J. Capstick, D.J. McPhail, D.E. Pooley, G.D. Howells, G. Gorini, F. Fernandez-
879 Alonso, The neutron guide upgrade of the TOSCA spectrometer, *Nucl. Instruments*
880 *Methods Phys. Res. Sect. A Accel. Spectrometers, Detect. Assoc. Equip.* 896 (2018) 68–74.
881 <https://doi.org/10.1016/j.nima.2018.04.009>.
- 882 [49] O. Arnold, J.C. Bilheux, J.M. Borreguero, A. Buts, S.I. Campbell, L. Chapon, M. Doucet, N.
883 Draper, R. Ferraz Leal, M.A. Gigg, V.E. Lynch, A. Markvardsen, D.J. Mikkelson, R.L.
884 Mikkelson, R. Miller, K. Palmen, P. Parker, G. Passos, T.G. Perring, P.F. Peterson, S. Ren,
885 M.A. Reuter, A.T. Savici, J.W. Taylor, R.J. Taylor, R. Tolchenov, W. Zhou, J. Zikovsky,
886 Mantid—Data analysis and visualization package for neutron scattering and μ SR
887 experiments, *Nucl. Instruments Methods Phys. Res. Sect. A Accel. Spectrometers, Detect.*
888 *Assoc. Equip.* 764 (2014) 156–166.
889 <https://doi.org/https://doi.org/10.1016/j.nima.2014.07.029>.
- 890 [50] S. Plimpton, Fast parallel algorithms for short-range molecular dynamics, *J. Comput.*
891 *Phys.* 117 (1997) 1–42. <https://doi.org/https://doi.org/10.1006/jcph.1995.1039>.
- 892 [51] H.J.C. Berendsen, J.R. Grigera, T.P. Straatsma, The missing term in effective pair potentials,
893 *J. Phys. Chem.* 91 (1987) 6269–6271.
894 <https://doi.org/https://doi.org/10.1021/j100308a038>.
- 895 [52] R.T. Cygan, J.J. Liang, A.G. Kalinichev, Molecular models of hydroxide, oxyhydroxide, and
896 clay phases and the development of a general force field, *J. Phys. Chem. B.* 108 (2004)
897 1255–1266. <https://doi.org/https://doi.org/10.1021/jp0363287>.

- 898 [53] R.T. Cygan, J.A. Greathouse, A.G. Kalinichev, Advances in Clayff molecular simulation of
899 layered and nanoporous materials and their aqueous interfaces, *J. Phys. Chem. C.* 125
900 (2021) 17573–17589. <https://doi.org/10.1021/acs.jpcc.1c04600>.
- 901 [54] J. Wang, A.G. Kalinichev, R.J. Kirkpatrick, R.T. Cygan, Structure, energetics, and dynamics
902 of water adsorbed on the muscovite (001) surface: a molecular dynamics simulation., *J.*
903 *Phys. Chem. B.* 109 (2005) 15893–15905.
904 <https://doi.org/https://doi.org/10.1021/jp045299c>.
- 905 [55] I.C. Bourg, G. Sposito, Molecular dynamics simulations of the electrical double layer on
906 smectite surfaces contacting concentrated mixed electrolyte (NaCl-CaCl(2)) solutions, *J.*
907 *Colloid Interface Sci.* 360 (2011) 701–715.
908 <https://doi.org/https://doi.org/10.1016/j.jcis.2011.04.063>.
- 909 [56] I.C. Bourg, C.I. Steefel, Molecular dynamics simulations of water structure and diffusion in
910 silica nanopores, *J. Phys. Chem. C.* 116 (2012) 11556–11564.
911 <https://doi.org/https://doi.org/10.1021/jp301299a>.
- 912 [57] E. Ferrage, B. Lanson, L.J. Michot, J.L. Robert, Hydration properties and interlayer
913 organization of water and ions in synthetic Na-smectite with tetrahedral layer charge.
914 Part 1. Results from X-ray diffraction profile modeling, *J. Phys. Chem. C.* 114 (2010)
915 4515–4526. <https://doi.org/https://doi.org/10.1021/jp909860p>.
- 916 [58] N.W. Ockwig, R.T. Cygan, L.J. Criscenti, T.M. Nenoff, Molecular dynamics studies of
917 nanoconfined water in clinoptilolite and heulandite zeolites, *Phys. Chem. Chem. Phys.* 10
918 (2008) 800–807. <https://doi.org/https://doi.org/10.1039/B711949F>.
- 919 [59] O.M. Roscioni, L. Muccioli, C. Zannoni, Predicting the Conditions for Homeotropic
920 Anchoring of Liquid Crystals at a Soft Surface. 4-n-Pentyl-4'-cyanobiphenyl on Alkylsilane
921 Self-Assembled Monolayers, *ACS Appl. Mater. Interfaces.* 9 (2017) 11993–12002.
922 <https://doi.org/https://doi.org/10.1021/acsami.6b16438>.
- 923 [60] A. Fernandez-Martinez, J. Tao, A.F. Wallace, I.C. Bourg, M.R. Johnson, J.J. De Yoreo, G.
924 Sposito, G.J. Cuello, L. Charlet, Curvature-induced hydrophobicity at imogolite-water
925 interfaces, *Environ. Sci. Nano.* 7 (2020) 2759–2772.
926 <https://doi.org/https://doi.org/10.1039/D0EN00304B>.
- 927 [61] A.A. Skelton, P. Fenter, J.D. Kubicki, D.J. Wesolowski, P.T. Cummings, Simulations of the
928 quartz(1011)/water interface: A comparison of classical force fields, Ab initio molecular
929 dynamics, and X-ray reflectivity experiments, *J. Phys. Chem. C.* 115 (2011) 2076–2088.
930 <https://doi.org/https://doi.org/10.1021/jp109446d>.

- 931 [62] E. Ferrage, B.A. Sakharov, L.J. Michot, A. Delville, A. Bauer, B. Lanson, S. Grangeon, G.
932 Frapper, M. Jiménez-Ruiz, G.J. Cuello, Hydration properties and interlayer organization of
933 water and ions in synthetic Na-smectite with tetrahedral layer charge. Part 2. Toward a
934 precise coupling between molecular simulations and diffraction data, *J. Phys. Chem. C.*
935 115 (2011) 1867–1881. <https://doi.org/https://doi.org/10.1021/jp105128r>.
- 936 [63] M.C.F. Wander, A.E. Clark, Structural and dielectric properties of quartz - Water
937 interfaces, *J. Phys. Chem. C.* 112 (2008) 19986–19994.
938 <https://doi.org/https://doi.org/10.1021/jp803642c>.
- 939 [64] T.R. Underwood, I.C. Bourg, Large-scale molecular dynamics simulation of the
940 dehydration of a suspension of smectite clay nanoparticles, *J. Phys. Chem. C.* 124 (2020)
941 3702–3714. <https://doi.org/https://doi.org/10.1021/acs.jpcc.9b11197>.
- 942 [65] M.A. Etzold, P.J. McDonald, A.F. Routh, Growth of sheets in 3D confinements — a model
943 for the C–S–H meso structure, *Cem. Concr. Res.* 63 (2014) 137–142.
944 <https://doi.org/https://doi.org/10.1016/j.cemconres.2014.05.001>.
- 945 [66] H.M. Jennings, Refinements to colloid model of C-S-H in cement : CM-II, 38 (2008) 275–
946 289. <https://doi.org/10.1016/j.cemconres.2007.10.006>.
- 947 [67] G. Goret, B. Aoun, E. Pellegrini, MDANSE: An Interactive Analysis Environment for
948 Molecular Dynamics Simulations, *J. Chem. Inf. Model.* 57 (2017) 1–5.
949 <https://doi.org/10.1021/acs.jcim.6b00571>.
- 950 [68] B. Lothenbach, A. Nonat, Calcium silicate hydrates: Solid and liquid phase composition,
951 *Cem. Concr. Res.* 78 (2015) 57–70.
952 <https://doi.org/https://doi.org/10.1016/j.cemconres.2015.03.019>.
- 953 [69] E. L'Hôpital, B. Lothenbach, G. Le Saout, D. Kulik, K. Scrivener, Incorporation of
954 aluminium in calcium-silicate-hydrates, *Cem. Concr. Res.* 75 (2015) 91–103.
955 <https://doi.org/https://doi.org/10.1016/j.cemconres.2015.04.007>.
- 956 [70] I.G. Richardson, The calcium silicate hydrates, *Cem. Concr. Res.* 38 (2008) 137–158.
957 <https://doi.org/https://doi.org/10.1016/j.cemconres.2007.11.005>.
- 958 [71] E. L'Hôpital, B. Lothenbach, D.A. Kulik, K. Scrivener, Influence of calcium to silica ratio on
959 aluminium uptake in calcium silicate hydrate, *Cem. Concr. Res.* 85 (2016) 111–121.
960 <https://doi.org/https://doi.org/10.1016/j.cemconres.2016.01.014>.
- 961 [72] A.J. Allen, J.J. Thomas, H.M. Jennings, Composition and density of nanoscale calcium-
962 silicate-hydrate in cement, *Nat. Mater.* 6 (2007) 311–316.

- 963 <https://doi.org/https://doi.org/10.1038/nmat1871>.
- 964 [73] S.J. Gregg, K.S.W. Sing, H.W. Salzberg, Adsorption surface area and porosity, J.
965 Electrochem. Soc. 114 (1967) 279C. <https://doi.org/10.1149/1.2426447>.
- 966 [74] J. Thomas, H. Jennings, A. Allen, The surface area of hardened cement paste as measured
967 by various techniques, *Concr. Sci. Eng.* 1 (1999).
968 [http://www.civil.northwestern.edu/people/thomas/pdf/Thomas_SAreview_CSE_1999.p](http://www.civil.northwestern.edu/people/thomas/pdf/Thomas_SAreview_CSE_1999.pdf)
969 [df](http://www.civil.northwestern.edu/people/thomas/pdf/Thomas_SAreview_CSE_1999.pdf).
- 970 [75] R.S. Mikhail, A.M. Kamel, S.A. Abo-El-Enein, Surface properties of cement hydration
971 products. I. Pore structure of calcium silicate hydrates prepared in a suspension form, J.
972 *Appl. Chem.* 19 (1969) 324–328. <https://doi.org/10.1002/jctb.5010191105>.
- 973 [76] R. Badmann, N. Stockhausen, M.J. Setzer, The statistical thickness and the chemical
974 potential of adsorbed water films, *J. Colloid Interface Sci.* 82 (1981) 534–542.
975 [https://doi.org/10.1016/0021-9797\(81\)90395-7](https://doi.org/10.1016/0021-9797(81)90395-7).
- 976 [77] A.A. Levchenko, A.I. Kolesnikov, N.L. Ross, J. Boerio-Goates, B.F. Woodfield, G. Li, A.
977 Navrotsky, Dynamics of water confined on a TiO₂ (anatase) surface, *J. Phys. Chem. A.* 111
978 (2007) 12584–12588. <https://doi.org/10.1021/jp076033j>.
- 979 [78] P.C.H. Mitchell, S.F. Parker, A.J. Ramirez-Cuesta, J. Tomkinson, *Vibrational Spectroscopy*
980 *with Neutrons*, in: *Ser. Neutron Tech. Appl.*, WORLD SCIENTIFIC, 2005: p. 668.
981 <https://doi.org/doi:10.1142/5628>.
- 982 [79] M. Jiménez-Ruiz, E. Ferrage, M. Blanchard, J. Fernandez-Castanon, A. Delville, M.R.
983 Johnson, L.J. Michot, Combination of Inelastic Neutron Scattering Experiments and ab
984 Initio Quantum Calculations for the Study of the Hydration Properties of Oriented
985 Saponites, *J. Phys. Chem. C.* 121 (2017) 5029–5040.
- 986 [80] D. Russo, J. Teixeira, L. Kneller, J.R.D. Copley, J. Ollivier, S. Perticaroli, E. Pellegrini, M.A.
987 Gonzalez, Vibrational density of states of hydration water at biomolecular sites:
988 Hydrophobicity promotes low density amorphous ice behavior, *J. Am. Chem. Soc.* 133
989 (2011) 4882–4888. <https://doi.org/10.1021/ja109610f>.
- 990 [81] G. Monet, E. Paineau, Z. Chai, M.S. Amara, A. Orecchini, M. Jimenéz-Ruiz, A. Ruiz-Caridad,
991 L. Fine, S. Rouzière, L.M. Liu, G. Teobaldi, S. Rols, P. Launois, Solid wetting-layers in
992 inorganic nano-reactors: The water in imogolite nanotube case, *Nanoscale Adv.* 2 (2020)
993 1869–1877. <https://doi.org/10.1039/d0na00128g>.
- 994 [82] E.F. Sheka, K. Hołderna-Natkaniec, I. Natkaniec, J.X. Krawczyk, Y.A. Golubev, N.N.

- 995 Rozhkova, V. V. Kim, N.A. Popova, V.A. Popova, Computationally Supported Neutron
996 Scattering Study of Natural and Synthetic Amorphous Carbons, *J. Phys. Chem. C*. 123
997 (2019) 15841–15850. <https://doi.org/10.1021/acs.jpcc.9b03675>.
- 998 [83] S.R. Larsen, L. Michels, É.C. dos Santos, M.C. Berg, W.P. Gates, L.P. Aldridge, T. Seydel, J.
999 Ollivier, M.T.F. Telling, J.O. Fossum, H.N. Bordallo, Physicochemical characterisation of
1000 fluorohectorite: Water dynamics and nanocarrier properties, *Microporous Mesoporous*
1001 *Mater.* 306 (2020) 110512. <https://doi.org/10.1016/j.micromeso.2020.110512>.
- 1002 [84] S.H. Chen, C. Liao, F. Sciortino, P. Gallo, P. Tartaglia, Model for single-particle dynamics in
1003 supercooled water, *Phys. Rev. E*. 59 (1999) 6708–6714.
1004 <https://doi.org/10.1103/PhysRevE.59.6708>.
- 1005 [85] R.T. Cygan, L.L. Daemen, A.G. Ilgen, J.L. Krumhansl, T.M. Nenoff, Inelastic neutron
1006 scattering and molecular simulation of the dynamics of interlayer water in smectite clay
1007 minerals, *J. Phys. Chem. C*. 119 (2015) 28005–28019.
1008 <https://doi.org/10.1021/acs.jpcc.5b08838>.
- 1009 [86] D.C. Elton, M. Fernández-Serra, The hydrogen-bond network of water supports
1010 propagating optical phonon-like modes, *Nat. Commun.* 7 (2016) 10193.
1011 <https://doi.org/10.1038/ncomms10193>.
- 1012 [87] T. Zhou, K. Ioannidou, F.-J. Ulm, M.Z. Bazant, R.J.M. Pellenq, Multiscale poromechanics of
1013 wet cement paste, *Proc. Natl. Acad. Sci.* 116 (2019) 10652–10657.
- 1014 [88] P.A. Bonnaud, B. Coasne, R.J.M. Pellenq, Solvated calcium ions in charged silica
1015 nanopores, *J. Chem. Phys.* 137 (2012). <https://doi.org/10.1063/1.4742854>.
- 1016 [89] I. Odler, The BET-specific surface area of hydrated Portland cement and related
1017 materials, 33 (2003) 2049–2056. [https://doi.org/https://doi.org/10.1016/S0008-](https://doi.org/https://doi.org/10.1016/S0008-8846(03)00225-4)
1018 [8846\(03\)00225-4](https://doi.org/https://doi.org/10.1016/S0008-8846(03)00225-4).
- 1019 [90] J. Beaudoin, I. Odler, Hydration, setting and hardening of Portland cement, in: P. Hewlett,
1020 M. Liska (Eds.), *Lea's Chem. Cem. Concr.*, 5th ed., Elsevier Ltd., Oxford, U.K., 2019: pp.
1021 157–250. <https://doi.org/10.1016/B978-075066256-7/50018-7>.
- 1022 [91] S. Grangeon, F. Claret, C. Lerouge, F. Warmont, T. Sato, S. Anraku, C. Numako, Y. Linard, B.
1023 Lanson, On the nature of structural disorder in calcium silicate hydrates with a
1024 calcium/silicon ratio similar to tobermorite, *Cem. Concr. Res.* 52 (2013) 31–37.
1025 <https://doi.org/https://doi.org/10.1016/j.cemconres.2013.05.007>.
- 1026 [92] B. Li, N. Li, H.J.H. Brouwers, Q. Yu, W. Chen, Understanding hydrogen bonding in calcium

- 1027 silicate hydrate combining solid-state NMR and first principle calculations, *Constr. Build.*
1028 *Mater.* 233 (2020) 117347.
1029 <https://doi.org/https://doi.org/10.1016/j.conbuildmat.2019.117347>.
- 1030 [93] S. Grangeon, F. Claret, C. Roosz, T. Sato, S. Gaboreau, Y. Linard, Structure of
1031 nanocrystalline calcium silicate hydrates: Insights from X-ray diffraction, synchrotron X-
1032 ray absorption and nuclear magnetic resonance, *J. Appl. Crystallogr.* 49 (2016) 771–783.
1033 <https://doi.org/10.1107/S1600576716003885>.
- 1034 [94] X. Cong, R.J. Kirkpatrick, $1\text{H} - 29\text{Si}$ CPMAS NMR study of the structure of calcium silicate
1035 hydrate, *Adv. Cem. Based Mater.* 3 (1996) 144–156.
1036 <https://doi.org/https://doi.org/10.1680/adcr.1995.7.27.103>.
- 1037 [95] M.P. Asta, A. Fernandez-Martinez, J. Alonso, L. Charlet, N. Findling, V. Magnin, B. Ruta, M.
1038 Sprung, F. Westermeier, Nanoscale Ion Dynamics Control on Amorphous Calcium
1039 Carbonate Crystallization: Precise Control of Calcite Crystal Sizes, *J. Phys. Chem. C.* 124
1040 (2020) 25645–25656. <https://doi.org/10.1021/acs.jpcc.0c08670>.
- 1041 [96] E.A. Pachon-Rodriguez, E. Guillon, G. Houvenaghel, J. Colombani, Wet creep of hardened
1042 hydraulic cements — Example of gypsum plaster and implication for hydrated Portland
1043 cement, *Cem. Concr. Res.* 63 (2014) 67–74.
1044 <https://doi.org/https://doi.org/10.1016/j.cemconres.2014.05.004>.
- 1045
- 1046